An investigation of shock-induced phase transition in soda-lime glass

Joshi, Akshay; Gandhi, Vatsa; Ravindran, Suraj; Ravichandran, Guruswami

Important note
To cite this publication, please use the final published version (if applicable).
Please check the document version above.

An investigation of shock-induced phase transition in soda-lime glass ꜰ

🆔 Akshay Joshi, 🆔 Vatsa Gandhi, 🆔 Suraj Ravindran, et al.

COLLECTIONS

Paper published as part of the special topic on Shock Behavior of Materials

ꜰ   This paper was selected as Featured

View Online   Export Citation   CrossMark

ARTICLES YOU MAY BE INTERESTED IN

A bright future for silicon in quantum technologies
Journal of Applied Physics **131**, 200901 (2022); https://doi.org/10.1063/5.0093822

Hot spot ignition and growth from tandem micro-scale simulations and experiments on plastic-bonded explosives
Journal of Applied Physics **131**, 205901 (2022); https://doi.org/10.1063/5.0085356

Oxide glasses under pressure: Recent insights from experiments and simulations
Journal of Applied Physics **131**, 170901 (2022); https://doi.org/10.1063/5.0088606

An investigation of shock-induced phase transition in soda-lime glass F

Akshay Joshi,[1,2,a)] (iD) Vatsa Gandhi,[1] (iD) Suraj Ravindran,[1] (iD) and Guruswami Ravichandran[1] (iD)

AFFILIATIONS

[1]Graduate Aerospace Laboratories, California Institute of Technology, Pasadena, California 91125, USA
[2]Delft University of Technology, 2628 CD Delft, The Netherlands

Note: This paper is part of the Special Topic on Shock Behavior of Materials.
[a)]**Author to whom correspondence should be addressed:** ajoshi@caltech.edu

ABSTRACT

There exists a large body of evidence from experiments and molecular dynamics simulations to suggest the occurrence of phase transitions in soda-lime glass (SLG) and other silica glasses subject to shock compression to pressures above 3 GPa. In light of these findings, the current work investigated the existence of phase transition in SLG using shock and release experiments. The experiments employed symmetric SLG–SLG impact to achieve complete unloading to zero stress after shock compression to stresses in the range of 3–7 GPa. The stress–strain response and the Lagrangian release wave speed behavior of SLG obtained from these experiments are seen to reveal a mismatch between the loading and unloading paths of the pressure–strain curve for the material, which serves as compelling evidence for the occurrence of a shock-induced phase transition in the material at relatively low pressures. Furthermore, the release wave speed vs strain data obtained from experiments were used to construct a methodology for modeling the shock and release behavior of SLG. This scheme implemented in numerical simulations was able to capture the release behavior of shock compressed SLG, for which a robust and satisfactory model was previously unavailable.

I. INTRODUCTION

Shock compression and release experiments involve subjecting a target material to high compressive stresses, using plate impact or laser driven ablation, and releasing it to study its loading and unloading response. This technique has been used to determine the strength of a material[1–4] and its Grüneisen parameter[5,6] at high pressures and strain rates. Shock and release experiments employ optical velocimetry techniques such as velocity interferometer system for any reflector (VISAR),[7] photon Doppler velocimetry (PDV),[8] or embedded stress and strain gauges to infer the stress–strain loading and unloading history of the target material.[9,10] Further details of inferring the stress–strain history of the target material from velocimetry data is provided in Sec. II.

Shock and release experiments have been conducted in previous works on soda-lime glass (SLG) and other silica glasses to determine their Hugoniot elastic limit (HEL)[11,12] or to study onset of phase transition in the material.[13] These studies on silica glasses like SLG and fused quartz observed a progressively stiffer release response for higher impact stresses. Possible causes for this

behavior are a gradual and irreversible phase transition occurring in these glasses or a regular elastic release behavior in the material. A more careful analysis of the release behavior of SLG and other silica glasses is essential to verify the existence and properties of phase transitions in the material. As will be seen in Sec. IV of this work, such an analysis would have to involve the pressure–strain curve of the material as opposed to just the stress–strain curve.

There are many anomalous properties associated with SLG and other silica glasses in the 4–6 GPa pressure regime. These silica glasses are known to undergo reduction in strength[14,15] and shear modulus[16] with increase in pressure up to 5 GPa. For pressures greater than 5 GPa, both strength and shear modulus increase with pressure. Additionally, for impact stresses between 4 and 10 GPa, SLG is observed to undergo a complete and sudden loss of spall strength behind a failure front that travels significantly slower than the compression wave. In the study by Joshi *et al.,*[17] this failure wave phenomenon was found to carry a significant densification similar to what would be expected of a first-order phase transition.[5] It was speculated that localized densifications effected by phase

transition in SLG were responsible for the observed failure wave phenomenon, i.e, the failure wave was postulated to be a shock-induced phase transition wave. Additional past studies, as discussed next, indicate a possibility of the onset of phase transitions and molecular rearrangements in silica glasses at pressures of 4–6 GPa. These phase transitions could be a cause for the anomalous properties of silica glasses observed at these pressures.

Silicon dioxide (SiO_2, silica), which forms a major constituent of SLG (∼73%) and other silica glasses, has many crystalline polymorphs such as α-quartz, coesite, and stishovite, all of which are denser than amorphous silica. The temperature–pressure phase diagram for SiO_2[18] indicates that α-quartz and coesite are the thermodynamically favored crystalline structures for SiO_2 for pressures of 4–6 GPa. The α-quartz to coesite phase transition, which causes a volumetric densification of 9%–10% and occurs at 3–4 GPa pressure,[19] is known to be kinetically hindered and slow.[20] Crystallization of the α-quartz phase, from amorphous silica, was not observed in previous shock compression experiments,[21,22] presumably because this transition is kinetically hindered at temperatures achieved in these experiments. However, laser-driven compression experiments on amorphous silica[21] seem to indicate the onset of transition from the amorphous phase to the stishovite phase at stresses of 4.7 GPa. More recent shock compression experiments[23] were also able to obtain visual evidence for the shock-induced nucleation of stishovite nanocrystals in soda-lime glass at stresses of around 7 GPa. Another recent work involving quasistatic compression of SLG nanopillars[24] also suggests the possibility of SLG transforming to a stiffer stishovite phase at stresses of around 5 GPa. Past quasi-static compression experiments[25] and molecular simulation studies[26] on amorphous SiO_2 also indicate the presence of an ice-like first-order transition from low density amorphous phase to high density amorphous phase at pressures of 3.6 GPa. In their work involving molecular dynamics simulation studies, Trachenko and Dove[27] attribute the observed anomalous change in rigidity of fused silica (FS), in the 3–5 GPa pressure regime, to a densification (increase in coordination number) in the amorphous silica network, effected by molecular rearrangements.

The objectives of the present work on SLG, in context of the aforementioned findings are as follows:

- To study the release behavior of shock compressed SLG, with a view toward discerning between the two possible mechanisms, phase transition and regular ductile behavior, that explain the stiffening of SLG's release with increase in impact stress.
- To develop a material model that adequately captures the release behavior of shock compressed SLG. There are no robust and satisfactory models available for this purpose yet.

The experiments in the current work are performed at impact stresses of 4–7 GPa to probe the existence and onset of phase transition in SLG in a pressure regime where the material is known to possess many anomalous properties. A salient feature of the current shock and release experiments in comparison to previous similar experiments on silica glasses[11,13,28] is that, for the first time, complete unloading to zero stress is achieved using symmetric SLG–SLG impact. This unloading to zero stress is critical to unequivocally verify the existence of permanent densification in

shock compressed SLG, which was reported in earlier works on SLG.[9,29]

II. MATERIALS AND METHODS

The normal plate impact experiments conducted in this work used either tungsten carbide (WC) or soda-lime glass (SLG) disks to impact SLG disk targets as shown in Fig. 1. The SLG disks were sourced from University Wafers, Inc., South Boston, MA, and had densities of $2480 \pm 10 \, kg/m^3$. The target SLG disks were 5 mm thick and 30 mm in diameter, while the impactor SLG disk was 3 mm thick and 30 mm in diameter. Both had an average surface roughness of less than 1 nm. Aluminum rings were glued to the disks as shown in Fig. 1 to facilitate trigger upon impact. A $0.5 \, \mu m$ thin aluminum layer was also deposited on the rear surface of the SLG target to provide a reflective coating for velocimetry measurements. The rear surface of the SLG was lightly scuffed with a 1200 grit sand-paper prior to aluminum deposition to obtain diffused reflections from the surface. This is done to avoid any significant loss in the intensity of light, received by the velocimetry probe, that might occur due to shock-induced changes of the rear surface. The WC impactor was of BC-00 grade and sourced from Basic Carbide Corporation, Lowber, PA, and had a density of $15\,480 \pm 100 \, kg/m^3$. The WC disk was 2 mm thick and 34 mm in diameter. Lithium fluoride crystal (LiF[100]) disks were used as windows in these experiments. These disks were 25.4 mm in diameter, 6.32 ± 0.01 mm in thickness, and were sourced from ASPHERA, Inc., Santa Cruz, CA. The LiF crystals had densities of $2640 \, kg/m^3$ and less than 2 degree misalignment between the <100> crystal axis and the disk axis. No anti-reflective coating was deposited on the LiF disks as Fresnel reflections from the rear surface of the LiF window do not interfere significantly with photon Doppler velocimetry (PDV) measurements.[30]

The velocity–time profile of the SLG–LiF[100] interface was obtained using PDV,[8] which employs a 1550 nm wavelength light
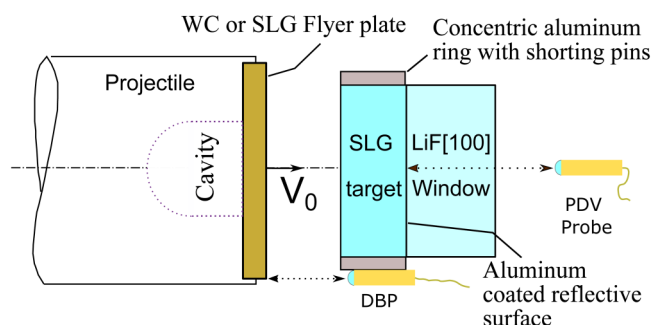
FIG. 1. Schematic of the plate impact experiment used to study the shock compression and release behavior of SLG using photon Doppler velocimetry (PDV). The Down–Barrel probe (DBP) measures the velocity of the impactor. The presence of the LiF[100] window ensures that the SLG remains under compression as the PDV probe records the SLG–LiF interface velocity. A $0.5 \, \mu m$ thick aluminum coating provides a reflective surface for PDV measurement. The cavity behind the impactor ensures that the stress releases to zero at the rear surface of the impactor.

FIG. 2. Schematic of procedure to evaluate the wave speed in material frame, $C_h(u)$. When impactors other than SLG are used (such as WC), one must account for the multiple reverberations in the impactor plate. L_I and L_t are the thicknesses of the impactor and target, respectively. t is the arrival time of the wave and $t = 0$ is the time of impact.
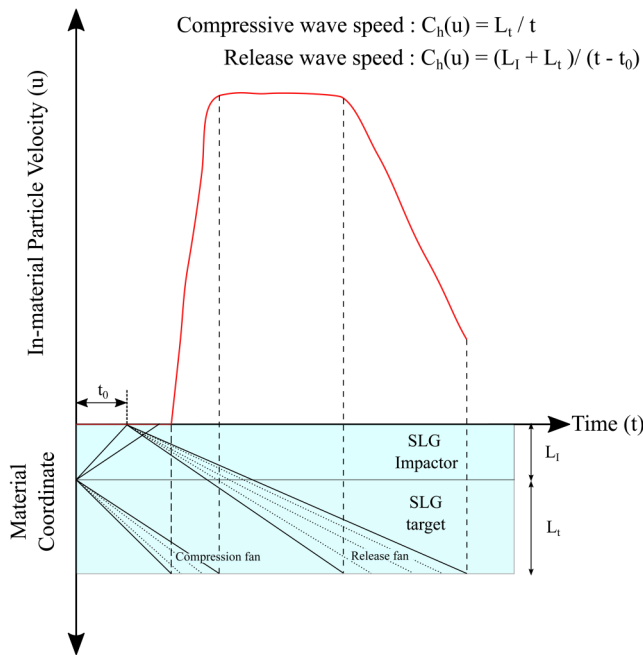
to probe the interface. Due to the presence of the LiF[100] window, appropriate optical and impedance mismatch corrections are applied to the observed velocity profile to obtain the in-material particle velocity using the procedure described by Joshi.[31] Furthermore, the in-material velocity profile thus obtained is used to construct the stress–strain loading history of the SLG target for which the following differential equations are integrated:[5,32]

$$d\varepsilon = \frac{du}{C_h(u)}, \tag{1}$$

$$d\sigma = \rho_0\, C_h(u)\, du, \tag{2}$$

where σ and ε are the axial stress and strain, respectively, $C_h(u)$ is the wave speed in material frame and u is the particle velocity in the target material, which is initially at rest. All compressive strains are defined to be positive in this work. $C_h(u)$, and u are obtained from the in-material particle velocity data as illustrated in Fig. 2.[31] The time t_0, as shown in Fig. 2, corresponds to the arrival of the compressive wave at the rear surface of the impactor. For the scope of this work, the entire release fan is assumed to originate from this point ($X = 0$, $t = t_0$) in the material position–time (X–t) diagram. This is an approximation that provides accurate results for wave profiles with small compressive fans. The accuracy of this method can be verified using results from experiments involving impact stresses much less than the HEL of the material.

The only significant source of uncertainty in the computed stress–strain profile is the time of trigger,[33] which can be caused by a tilt in impact. For the experiments conducted in this work, the tilt was lower than 1.5 mrad (0.086 degrees). Further details about computing the uncertainties in stress are outlined in the Appendix.

III. RESULTS AND DISCUSSION

The impact velocities, stresses, and other details corresponding to each plate impact experiment are summarized in Table I. The uncertainties in particle velocities were computed using the procedure outlined by Dolan.[34] The procedure for computing the uncertainties in stresses are outlined in the Appendix. The in-material velocities are computed by correcting for the impedance mismatch between SLG and LiF[100].[31]

The shock and release experiments, which involved peak axial stresses of 3–7 GPa, were conducted to probe the release behavior of SLG at stresses corresponding to the onset of the failure wave phenomenon, which is suspected to be caused by a localized phase transition in the material.[17,35]

A. Experiment No. WSL-1

Experiment No. WSL-1 involved impacting a 2 mm thick WC disk onto a 5 mm thick SLG disk target. Since the timings of reverberations of the stress-waves in the WC impactor were accurately observed by velocimetry of the WC–SLG interface in experiment No. AJ-2 of a previous work,[17] the impactor thickness and velocity were chosen to replicate that experiment, except now with the presence of the LiF window. These reverberation timings were then used to determine the speeds of the release waves arriving at the SLG–LiF interface. A plot of the observed and optically corrected interface velocity alongside a material position-time diagram is

TABLE I. Summary of shock compression and release experiments on soda-lime glass.

Experiment No.	Impactor	Thickness (mm)	Impact velocity (m/s)	Target thickness (mm)	Peak interface velocity (m/s) (optically corrected)	Peak in-material velocity (m/s)	Peak stress (GPa)
WSL-1	WC	2	N/A	5	411.5 ± 0.51	424.1	5.68 ± 0.26
SSL-2	SLG	3	1266.1 ± 2.40	5	523.3 ± 0.03	577.3	7.27 ± 0.25
SSL-3	SLG	3	879.6 ± 0.79	5	393.8 ± 0.53	411.1	5.51 ± 0.19
SSL-4	SLG	3	462.7 ± 2.14	5	230.9 ± 0.98	231.2	3.14 ± 0.13

shown in Fig. 3. The measured interface velocity can be seen to consist of high frequency oscillations, which become more pronounced after the first and second unloadings. This noise can be attributed to a reduction in the intensity of the light reflected back to the PDV and were excluded from the velocity measurements in order to accurately capture the stress–strain response of SLG. The optically corrected data were thus smoothened, by interpolation, to remove these oscillations while retaining the important features in the data such as the two-wave structures of the first and second release. The stress–strain curve for this experiment, constructed from the smoothened interface velocity using the procedure outlined in Sec. II [Eqs. (1) and (2)], is shown in Fig. 4. The peak compressive stress is computed to be 5.68 GPa, after which the unloading is observed to occur in multiple steps, each effected by the reverberation of the release waves in the WC impactor. The release wave speeds for the second release fan are computed using point B (see Fig. 3) as the origin of the second release fan. The time coordinate of points A and B are determined by using the velocimetry results from Expt. No. AJ-2 in Joshi et al.,[17] which used a WC impactor of almost identical thickness.

A significant observation is that the loading and unloading paths do not coincide. The unloading occurs only partially, up to a
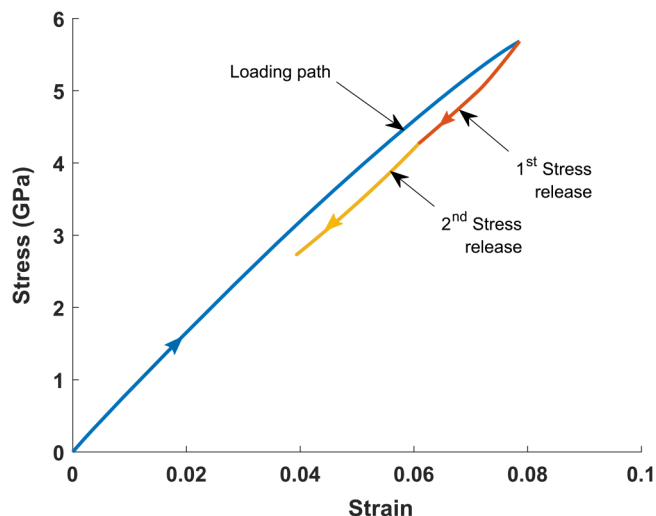

FIG. 4. Stress–strain curve for SLG deduced from experiment No. WSL-1. The uniaxial strain is also identical to the volumetric strain $\left(1 - \frac{\rho_0}{\rho}\right)$.

stress of around 2.8 GPa, due to the use of an impactor (WC) with impedance higher than the SLG target. However, the second unloading can be seen to proceed parallel to the loading curve. It can, thus, be assumed that a complete unloading would have resulted in a permanent densification in the material. It is very unlikely that this small hysteresis is due to onset of inelasticity in the material, as a small hysteresis would require a small yield strength for the material at these stresses, which would further entail an unlikely and abrupt increase in pressure due to a reduced deviatoric stress. As will be discussed later (Sec. IV), this observed hysteresis in the stress–strain curve is more likely due to a hysteresis in the pressure loading and unloading effected by a gradual phase transition occurring in the material.

The impact velocity could not be measured in this experiment due to the lack of light reflected back to the Down–Barrel probe (DBP). Although this impact velocity was not necessary to construct the stress–strain curve for the experiment, a consequence of not knowing the impact velocity is that the existence and extent of densification due to the failure wave, expected in SLG at these stresses, cannot be estimated. As was shown in Joshi et al.,[17] the densification due to the failure wave is associated with a difference between the observed and expected peak velocity. Without knowledge of the impact velocity, the expected peak velocity and hence the deficit in velocity cannot be estimated. As will be discussed later, numerical simulations of this experiment were able to match the observed peak velocity by considering an impact velocity of 490 m/s.

Additionally, due to reflections from the rear surface of the LiF window, the PDV probe was able to record the velocity–time history of the rear surface of LiF as well. Velocity measurements of the LiF-free surface indicate a spall occurring in the LiF material, which could be a possible reason for the loss of signal at later times from the SLG–LiF interface. The peak velocity for the LiF rear
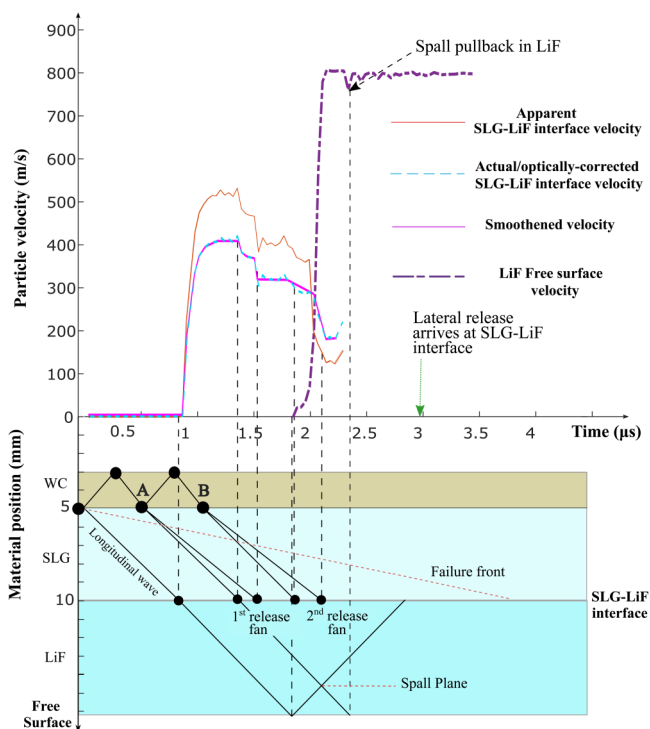

FIG. 3. Velocimetry data from experiment No. WSL-1 for SLG–LiF interface and LiF[100] free surface. A failure wave velocity of 1.3 km/s was assumed in constructing the material position-time (X–t) diagram.[17] The points A and B correspond to the arrival of the first and second reverberations of the release wave, respectively, at the WC–SLG interface.

surface can be seen to be approximately twice the optically corrected peak interface velocity, thus lending further credibility to the optical corrections applied to the observed interface velocity.

B. Experiment No. SSL-2

Experiment No. SSL-2 involved symmetric impact between a 3 mm thick SLG disk onto a 5 mm thick SLG disk target at an impact velocity of 1266 m/s. The SLG target is backed by a 6.5 mm thick LiF[100] window. A plot of the observed and optically corrected SLG–LiF interface velocity alongside a material position–time diagram is shown in Fig. 5, which is used to construct the stress–strain curve shown in Fig. 6. The peak compressive stress is computed to be 7.27 GPa. It can also be observed that complete unloading of stress to 0 GPa is achieved in this experiment, with a major part of the unloading curve parallel to the loading curve. It is, thus, observed that SLG retains a permanent (residual) volumetric strain of around 2%, which is higher than the permanent strain observed in experiment No. WSL-1.

The observed peak velocity for the LiF-free surface can again be seen to be approximately twice the optically corrected peak value for the interface velocity, thus lending further credibility to the optical corrections applied to the observed data. A significant observation can be made in the SLG–LiF interface velocity data
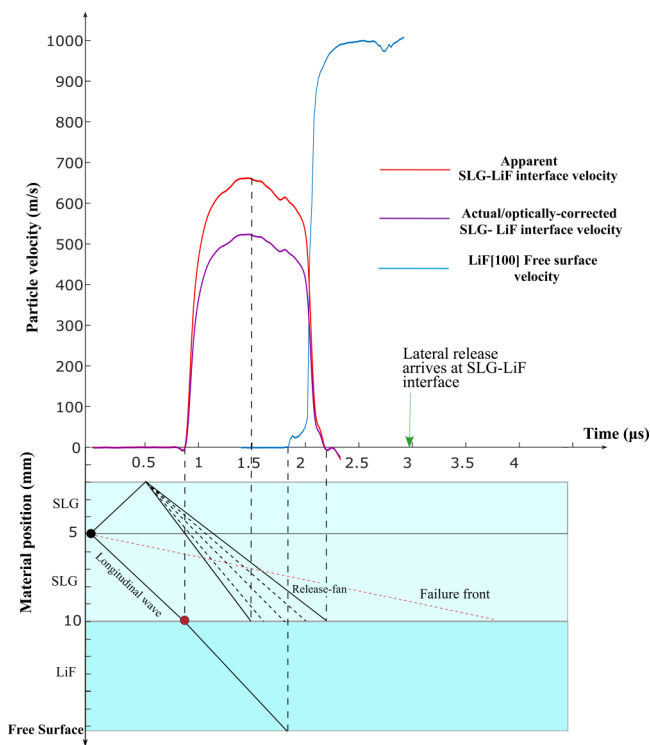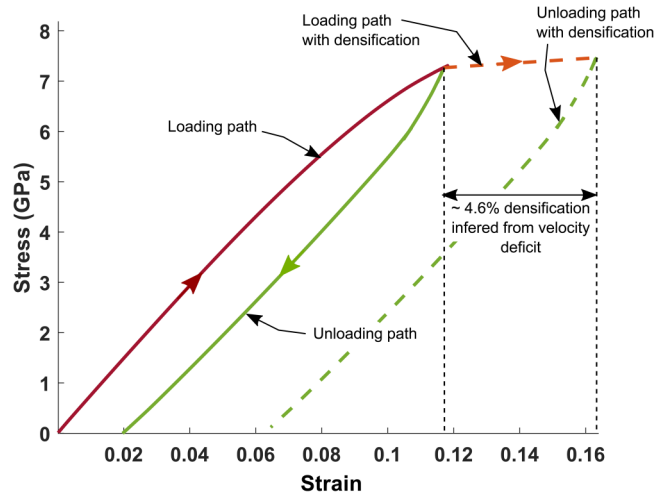

FIG. 6. Stress–strain curve for SLG material inferred from experiment No. SSL-2 not accounting and accounting for densification due to the failure wave. The uniaxial strain is also identical to the volumetric strain $\left(1 - \frac{\rho_0}{\rho}\right)$.

after they have been corrected for optical effects and impedance mismatch between SLG and LiF. The resultant in-material particle velocity can be seen to have a peak value of 577.3 m/s. This is around 56 m/s smaller than 633 m/s, which would be the expected peak velocity for symmetric SLG–SLG impact. This deficit occurs due to a fast traveling release wave that arrives at the SLG–LiF interface at 1.5 μs, thereby quenching/attenuating any compression wave that travels slower than 3.3 km/s. These slower traveling waves can be due to the inelastic (plastic) behavior of the SLG, which gives rise to a slower plastic shock wave, or due to the failure wave traveling at 1.3 km/s.[17] Thus, depending on the speed of this second wave and the observed deficit in peak velocity, an additional 1.8%–4.6%[17] of volume densification/strain will have to be considered in the stress–strain curve. For further illustrations and calculations in this work, the additional densification will be assumed to be 4.6% in magnitude and taken to be caused by the failure wave. The stress–strain curve incorporating this densification is also shown in Fig. 6.

C. Experiment No. SSL-3

This experiment involved impacting a 5 mm thick SLG disk with a 3 mm thick SLG disk at 880 m/s impact velocity. The LiF [100] window used was 8 mm thick. The velocimetry data for the SLG–LiF interface and the LiF-free surface, obtained in this experiment, are shown in Fig. 7. The optically corrected SLG–LiF interface velocity is also shown in Fig. 7. Furthermore, the in-material particle velocity for SLG is calculated from the SLG–LiF interface velocity. These velocities are listed in Table I. A significant observation is that the SLG in-material particle velocity, which is expected to be exactly half of the impact velocity for symmetric impact, is around 30 m/s lower than expected. As discussed in Joshi et al.,[17] this deficit in velocity can be attributed to a phase

FIG. 5. Velocimetry data of experiment No. SSL-2 for SLG–LiF interface and LiF-free surface. A failure wave velocity of 1.3 km/s was assumed in the material position–time (X–t) diagram.
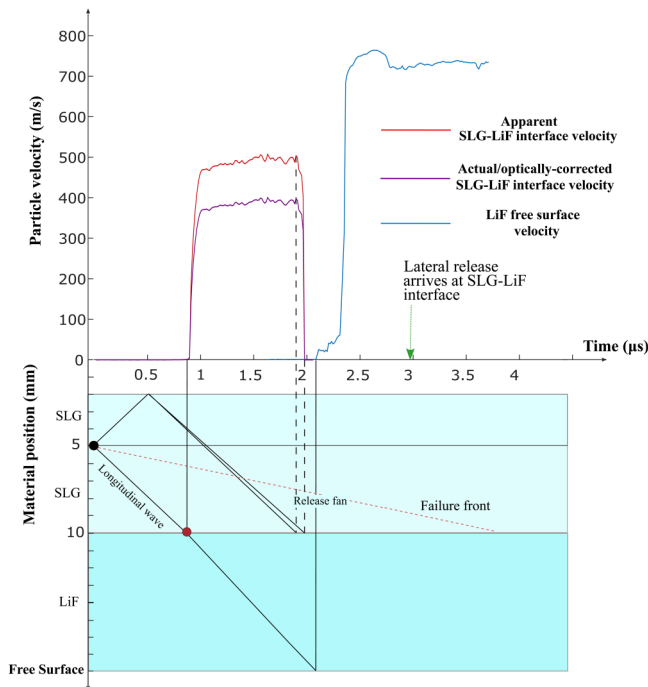
FIG. 7. Velocimetry data from experiment No. SSL-3 for the SLG–LiF interface and the LiF-free surface. A failure wave velocity of 1.3 km/s was assumed in the material position–time (X–t) diagram. Impact velocity is 879.6 m/s.

transition/densification in SLG, occurring at stresses of around 5 GPa. This densification causes an abrupt change in the slope of the stress–strain equation of state (EOS) of SLG and is observed as a slower traveling secondary compression wave. Joshi *et al.*[17] observed that, for SLG, this secondary wave, commonly referred to as the "failure wave," travels at a speed of around 1.3 km/s. As shown in the position–time (X–t) diagram in Fig. 7, this failure wave is too slow to be observed at the SLG–LiF interface, being attenuated by the longitudinal release wave from the rear surface of the SLG impactor.

The observed SLG–LiF interface velocity, after appropriate optical and impedance mismatch corrections, and analysis, reveals the peak stress attained in the SLG to be around 5.5 GPa, similar to what is observed in experiment No. WSL-1. The stress loading and unloading paths, inferred from the optically corrected SLG–LiF interface velocity, is shown in Fig. 8. The slope of and strain-change across the "densification" section of the loading–unloading plot are inferred by assuming the second wave's speed to be 1.3 km/s[17] (same as the failure wave). The existence and extent of this densification could not be verified in experiment No. WSL-1, as the impactor velocity was not known in that experiment.

The unloading can be seen to proceed along a slightly steeper path as compared to the loading path. A resultant mismatch between loading–unloading paths and permanent densification of over 2% can be observed in SLG.
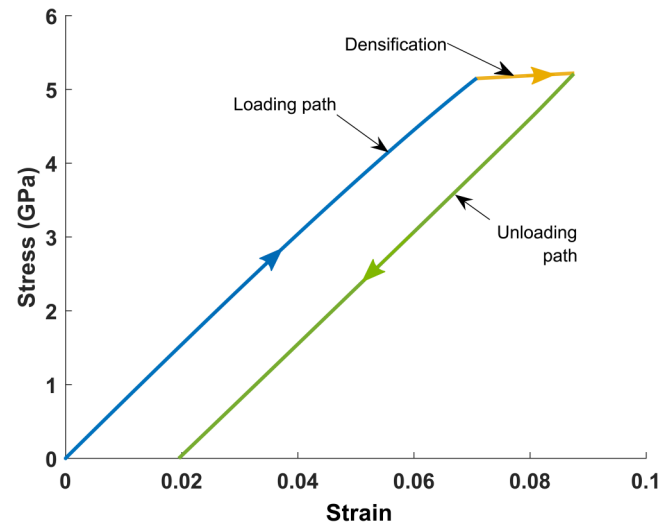

FIG. 8. Plot of stress–strain curve corresponding to experiment No. SSL-3. The uniaxial strain is also identical to the volumetric strain $\left(1 - \frac{\rho_0}{\rho}\right)$.

D. Experiment No. SSL-4

This experiment involved impacting a 5 mm thick SLG disk with a 3 mm thick SLG impactor with an impact velocity of 463 m/s. The LiF window used was 8 mm thick. The velocimetry data for the SLG–LiF interface and the LiF-free surface recorded for this experiment are shown in Fig. 9. Optical and impedance mismatch corrections are applied to the observed SLG–LiF interface velocity. The optically corrected SLG–LiF interface velocity is shown in Fig. 9, and the impedance corrected peak velocity is shown in Table I. A significant observation is that the impedance corrected (in-material) velocity is almost exactly half the impact velocity, as expected in a symmetric impact experiments. This observation serves as a verification of the densification inferred from the velocity deficit in experiment No. SSL-3 and also validates the optical correction scheme used in this work.[30,31]

The SLG–LiF interface velocity, corrected for optical path length change and impedance mismatch, was used to extract the stress–strain history of the SLG. The loading–unloading history for SLG is shown in Fig. 10, which suggests that the material behavior is nearly elastic. The peak compressive stress attained in the SLG target is computed using Eq. (2) to be 3.14 GPa. A minor mismatch between the loading and unloading paths, with a resulting minor permanent densification of around 0.3% can also be seen in Fig. 10.

E. Summary of experimental results

Figure 11 provides, in summary, a plot of SLG's stress–strain response for experiment Nos. WSL-1, SSL-2, SSL-3, SSL-4, AT-3, and AT-4. The interface–velocity data for experiments Nos. AT-3 and AT-4 were taken from Alexander *et al.*,[28] corrected for SLG–LiF impedance mismatch, and then processed to obtain the stress–strain curve shown in the plot. Experiment Nos. AT-3 and
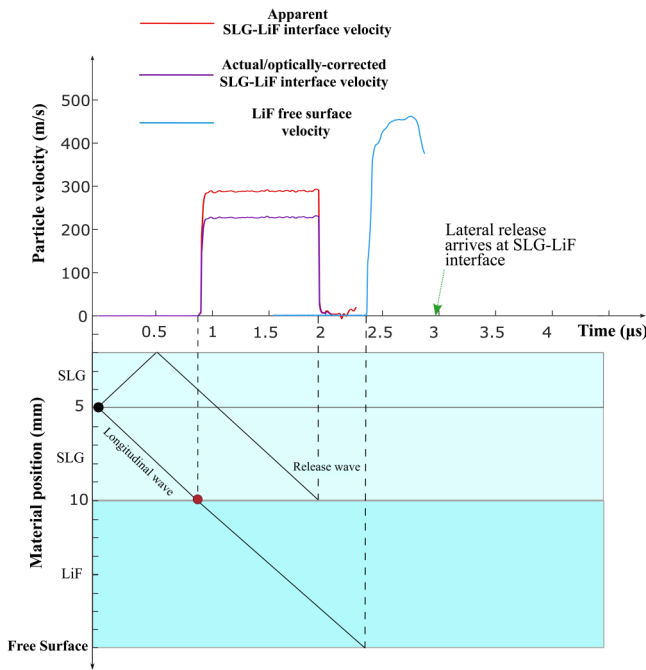
FIG. 9. Velocimetry data from experiment No. SSL-4 for the SLG–LiF interface and LiF-free surface. Impact velocity is 463 m/s.

FIG. 11. Summary of stress–strain response of SLG and pressure vs strain curves (isotherms) for polymorphs of silica (SiO_2), α-quartz, and coesite. SLG–LiF interface data for experiment Nos. AT-3 and AT-4 were taken from Ref. 28 and processed to obtain the shown stress–strain plots. EOS-1 is the equation of state for SLG used in Joshi *et al.*[17] Equations of state for α-quartz and coesite were taken from McWhan[39] and Hemley *et al.*,[18] respectively. The strains were computed using $\left(1 - \frac{\rho_0}{\rho}\right)$, with $\rho_0 = 2480 \, \text{kg/m}^3$.

AT-4 were chosen for analysis here as they too used symmetric SLG–SLG plate impact with LiF[100] windows for shock compression and release of SLG. Both Nos. AT-3 and AT-4 used 6 mm thick SLG impactors and targets. Experiment No. AT-3 was conducted at an impact velocity of 1.99 km/s, while experiment
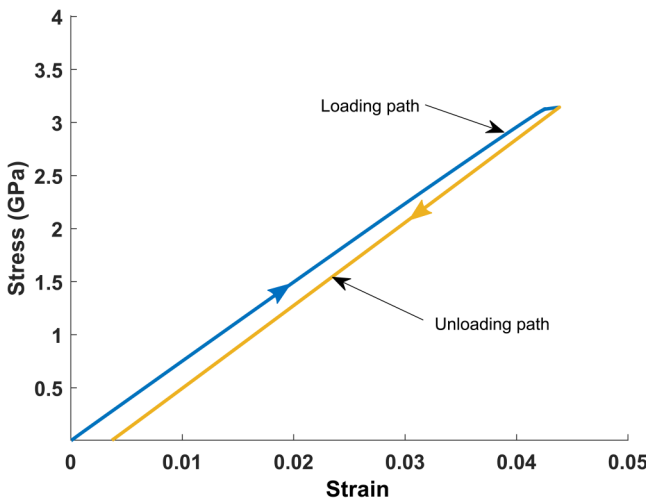

FIG. 10. Stress–strain plot for experiment No. SSL-4. The uniaxial strain is also identical to the volumetric strain $\left(1 - \frac{\rho_0}{\rho}\right)$.
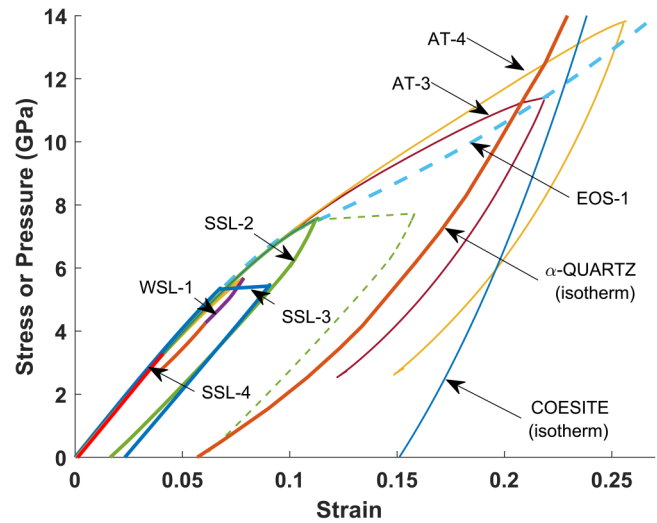
No. AT-4 was at an impact velocity of 2.38 km/s. Complete unloading to zero stress were not achieved in these experiments due to the use of a thick impactor, which delays the unloading wave traveling into the target from the impact surface. The use of an SLG impactor makes the velocity data more reliable for the purpose of extracting the stress–strain response. Due to the complete unloading to zero stress achieved in experiment Nos. SSL-2, SSL-3, and SSL-4, it can be observed that the loading–unloading hysteresis and permanent densification starts in SLG at an impact stress of around 5 GPa and continues to increase as the impact stress increases. The failure wave phenomenon, which is observed to occur in SLG that is shock compressed to stresses between 4.7 GPa[36,37] and 10.8 GPa,[17] seems to be correlated with the onset of the aforementioned loading–unloading hysteresis at 5 GPa. It was further observed in Joshi *et al.*[17] that failure waves carried an additional densification making them more reminiscent of phase transition waves.[35,38] Thus, the permanent densification and stress–strain hysteresis observed in the current work could be, in part or wholly, due to a phase transition occurring in SLG.

Figure 11 shows a plot of the observed stress–strain behavior of SLG alongside the pressure isotherms of α-quartz[39] and coesite.[18] Pressure isotherms of α-quartz and coesite were chosen for comparison, as opposed to stress Hugoniots for the respective materials, for a better approximation of the release (unloading) curve of the materials, which is generally isentropic and largely parallel to the pressure–strain curve.[5] For a material undergoing gradual, irreversible phase transition to a stiffer phase, the release

response is expected to become significantly stiffer with increasing peak compressive stresses. This can be partly attributed to the residual stiffer phase. It was postulated by Lacks,[26] through molecular dynamics simulations, that fused silica undergoes a transition to a stiffer high density amorphous phase at pressures of 3–5 GPa. It can also be noted that the unloading paths of SLG for experiment Nos. AT-3 and AT-4 closely resemble the pressure isotherm for α-quartz. With progressive stiffening, the release response of SLG can be expected to closely resemble the coesite isotherm. It is, therefore, very likely that SLG undergoes a localized transition[17] to one or more of these higher density phases at different stress levels. A more compelling evidence for shock-induced phase transition in SLG is discussed in Sec. IV. Additionally, from Fig. 11 it is evident that the hysteresis observed for Expt. No. SSL-4 is almost negligible, thereby validating the accuracy of the procedure employed to infer the stress–strain history of SLG from the velocimetry data.

Figure 12 provides a plot of the Lagrangian wave speeds of compression and release waves observed in SLG for experiment Nos. WSL-1, SSL-2, SSL-3, SSL-4, AT-3, and AT-4. The experimental observations for Lagrangian wave speeds in the present work seem to be in very good agreement with results of previous shock compression and release data for SLG.[11] From Fig. 12, it can be seen that for SLG, the onset of hysteresis occurs at a strain of 0.04, beyond which the compression and release wave speeds differ, and the strain corresponding to the HEL is around 0.1, beyond which the compression wave speeds increases with strain.
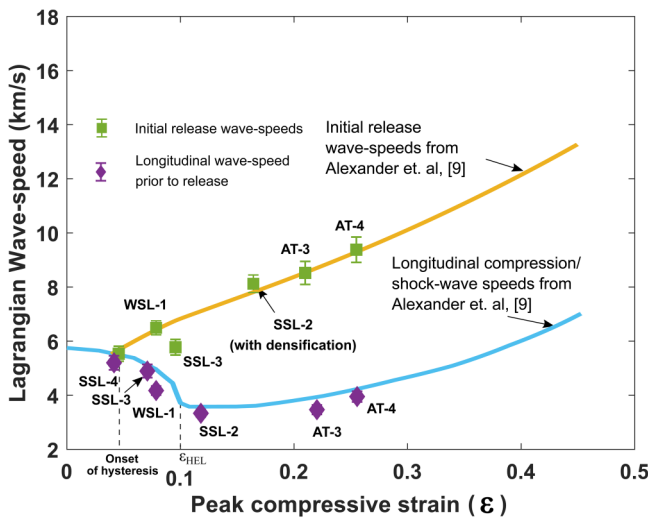
IV. PHASE TRANSITION IN SLG

Since, in general, plasticity is associated with the deviatoric stresses in the material, the pressure–volume equation of state (EOS) of the material can be assumed to be unaffected by inelastic behavior. Thus, for the case of a regular ductile material without phase transitions, neglecting the differences between the shock-Hugoniot and the release isentrope, the loading and unloading paths in the pressure–volume EOS can be assumed to be the

FIG. 12. Plot of Lagrangian wave speeds of compression and release waves in SLG. The data for experiments AT-3 and AT-4 are taken from Alexander *et al.*[28] The compression (blue line) and release (yellow line) wave speeds for SLG provided as a function of peak particle velocity in Alexander *et al.*[11] are plotted here as functions of strains (refer to the Appendix in Joshi *et al.*[17] for the procedure). The onset of hysteresis is the strain (0.04) at which the release and compression wave speeds start to differ significantly. The strain (ε) is computed as $\left(1 - \frac{\rho_0}{\rho}\right)$.

FIG. 13. Schematic stress–strain and pressure–strain diagrams of shock loading and release for materials with (a) regular inelastic response and (b) phase transition. The major difference in the two diagrams is the significant mismatch of the pressure vs strain loading and unloading paths for the latter case. The pressure–strain slope at release $\left(\frac{dp}{d\varepsilon}\right)_{release}$ can be seen to be higher compared to the slope at peak compression $\left(\frac{dp}{d\varepsilon}\right)_{loading}$. In both cases, material is assumed to lack strain hardening.

same. The pressure–strain and stress–strain behavior of a regular ductile material without phase transition is depicted in Fig. 13(a).

In contrast, a phase transition can be expected to alter the pressure–volume response of the material and give rise to a hysteresis in the pressure loading and unloading [see Fig. 13(b)]. Thus, a difference in loading and release paths in the pressure–volume EOS of the material would indicate a phase transition. As seen from Fig. 13(b), this difference in the two paths would be especially pronounced at the initial release, with the unloading pressure–strain response being significantly stiffer (higher slope) compared to the loading path, i.e, $\left(\frac{dp}{d\varepsilon}\right)_{release} > \left(\frac{dp}{d\varepsilon}\right)_{loading}$. This is consistent with the "flagpole" structure associated with the pressure (or stress)–strain curve of a material undergoing forward and reverse phase transition.[38] Furthermore, from Figs. 13(a) and 13(b), it can also be observed that for a material undergoing phase transition, at a given volumetric strain, the unloading pressure–strain path is generally stiffer (has a higher slope) compared to the loading pressure–strain path. In summary, any mismatch between the loading and unloading paths in the pressure–strain space (not just stress–strain space) is evidence for a pressure-induced phase transition in the material. The presence of such a mismatch in SLG and fused silica are demonstrated next.

A. Evaluating slopes of the loading and release pressure–strain curves using experimental data

A quantitative estimate of any mismatch between loading and unloading paths of the pressure–strain curve can be arrived at by knowing the evolution of shear modulus (G) of SLG as a function of pressure. For impact stresses above the HEL, the longitudinal compression and initial release wave speeds can be used to estimate the shear modulus of SLG as a function of peak strain (ε_{init}). The relationship between the initial release wave speed (C_R), shear modulus as a function of peak strain ($G(\varepsilon_{init})$), and the slope of the pressure–strain curve during initial release $\left(\frac{dp}{d\varepsilon}(\varepsilon_{init})\right)_{release}$ is discussed next.

Under conditions of uniaxial strain, prevalent in plate impact experiments, the longitudinal stress (σ), pressure (p), and the longitudinal/volumetric strain (ε) can be related as follows:[5]

$$\sigma = \begin{cases} p + \frac{4G\varepsilon}{3} & \varepsilon \leq \varepsilon_{HEL}, \\ p + \frac{2Y(\varepsilon_p)}{3} & \varepsilon > \varepsilon_{HEL}, \end{cases} \tag{3}$$

where $Y(\varepsilon_p)$ is the yield (flow) strength as a function of plastic strain.

When a material shock compressed to stresses and strains above its HEL undergoes release, its initial release will be elastic,[5] and it is described by the following equation:

$$\sigma(\varepsilon) = p(\varepsilon) + \frac{4G(\varepsilon)}{3}(\varepsilon - \varepsilon_{init} + \varepsilon_{HEL}), \tag{4}$$

where ε_{init} is the maximum compressive strain attained before unloading starts, as shown in Fig. 13(a). A prerequisite for Eq. (4)

is that $\varepsilon_{init} \geq \varepsilon_{HEL}$. Furthermore, differentiating Eq. (4) gives

$$\left(\frac{d\sigma}{d\varepsilon}(\varepsilon)\right)_{release} = \left(\frac{dp}{d\varepsilon}(\varepsilon)\right)_{release} + \frac{d}{d\varepsilon}\left(\frac{4G(\varepsilon)}{3}(\varepsilon - \varepsilon_{init} + \varepsilon_{HEL})\right). \tag{5}$$

The above equation, when evaluated at $\varepsilon = \varepsilon_{init}$, gives the initial elastic release wave speed: $C_R^2(\varepsilon_{init}) = \frac{1}{\rho_0}\frac{d\sigma}{d\varepsilon}(\varepsilon_{init})$. When evaluated at $\varepsilon = \varepsilon_{init}$, Eq. (5) thus simplifies to

$$\left(\frac{dp}{d\varepsilon}(\varepsilon_{init})\right)_{release} = \rho_0 C_R^2(\varepsilon_{init}) - \frac{4\varepsilon_{HEL}}{3}\left(\frac{dG}{d\varepsilon}(\varepsilon_{init}) + \frac{1}{\varepsilon_{HEL}}G(\varepsilon_{init})\right). \tag{6}$$

Regarding the above equation, it is important to note that the initial release wave speed, C_R, can be obtained from the velocimetry data (see Fig. 12) and the shear modulus, $G(\varepsilon)$, can be obtained from static/dynamic compression experiments that measure shear wave speeds.[16,40] The shear modulus is conventionally reported as a function of pressure (p)[16,40] and can be re-expressed as a function of strain (ε) for use in Eq. (6), by knowing the (loading) pressure–strain [$p(\varepsilon)$] relation for the material. The condition $\varepsilon_{init} \geq \varepsilon_{HEL}$ remains an important prerequisite for Eq. (6).

Thus, from experimentally observed data, it is possible to estimate $\left(\frac{dp}{d\varepsilon}(\varepsilon_{init})\right)_{release}$ using Eq. (6). The procedure to estimate $\left(\frac{dp}{d\varepsilon}(\varepsilon_{init})\right)_{loading}$ from experimentally available data is discussed next.

As shown in Fig. 13(a), for ductile materials with negligible strain hardening, the post-yield stress–strain and pressure–strain paths are parallel to a good approximation. Thus, for $\varepsilon_{init} \geq \varepsilon_{HEL}$, the slope of the stress Hugoniot $\left(\frac{d\sigma_h}{d\varepsilon}(\varepsilon_{init})\right)_{loading}$ approximately equals the slope of the loading pressure–strain curve $\left(\frac{dp}{d\varepsilon}(\varepsilon_{init})\right)_{loading}$.

For $\varepsilon_{init} \geq \varepsilon_{HEL}$, the slope of the stress Hugoniot $\frac{d\sigma_h}{d\varepsilon}$ is evaluated by considering the Rayleigh line and the corresponding equation for Hugoniot stresses (σ_h) higher than σ_{HEL},

$$\sigma_h - \sigma_{HEL} = \rho_0 U_S^2(\varepsilon)(\varepsilon - \varepsilon_{HEL}) \tag{7}$$

$$\implies \frac{d\sigma_h}{d\varepsilon} = \rho_0 U_S^2 + 2\rho_0 U_S \frac{dU_S}{d\varepsilon}(\varepsilon - \varepsilon_{HEL}), \tag{8}$$

where U_S is the shock speed. To evaluate $U_S(\varepsilon)$, the U_S–u_p relation, shown in Eq. (9), and used for SLG in previous works[11,17] can be used. The shock speed as function of particle velocity [$U_S(u_p)$] for SLG can be expressed as $U_S(\varepsilon)$ as follows (all velocities in km/s):

$$U_S(u_p) = 3.15 + 1.54(u_p - u_{pHEL}). \tag{9}$$

Using $\varepsilon - \varepsilon_{HEL} = \frac{u_p - u_{pHEL}}{U_S(u_p)}$, the above equation can be rewritten as

$$U_S(\varepsilon) = \frac{3.15}{1 - 1.54(\varepsilon - \varepsilon_{HEL})} \quad (10)$$

$$\implies \frac{dU_S}{d\varepsilon} = \frac{4.851}{(1 - 1.54(\varepsilon - \varepsilon_{HEL}))^2}. \quad (11)$$

Thus, Eq. (8) can be evaluated using Eqs. (10) and (11). Furthermore, noting that the slopes of the pressure–strain (loading) curve and the Hugoniot stress–strain curve are approximately the same (all pressures and stresses in GPa),

$$\left(\frac{dp}{d\varepsilon}(\varepsilon)\right)_{loading} = \frac{d\sigma_h}{d\varepsilon} = \rho_0\left(\frac{3.15}{1 - 1.54(\varepsilon - \varepsilon_{HEL})}\right)^2$$
$$+ 2\rho_0\left(\frac{3.15(\varepsilon - \varepsilon_{HEL})}{1 - 1.54(\varepsilon - \varepsilon_{HEL})}\right)$$
$$\times \left(\frac{4.851(\varepsilon - \varepsilon_{HEL})}{(1 - 1.54(\varepsilon - \varepsilon_{HEL}))^2}\right), \quad (12)$$

where $\varepsilon_{HEL} = 0.1$ for SLG (see Figs. 12 and 13).

Equations (6) and (12) thus provide estimates of the slopes of the release and loading pressure–strain curves for SLG. In order to validate these equations, and to illustrate the contrast in behavior between materials exhibiting phase transition and materials with regular ductile deformation, Sec. IV B discusses plots of $\left(\frac{dp}{d\varepsilon}(\varepsilon_{init})\right)_{release}$ and $\left(\frac{dp}{d\varepsilon}\right)_{loading}$ for a regular ductile material (without shock-induced phase transition) like 6061 aluminum alloy alongside the plots for SLG and pure form of amorphous silica, fused silica (FS).

B. Pressure–strain slope plots for Al6061, FS, and SLG

To evaluate $\left(\frac{dp}{d\varepsilon}(\varepsilon_{init})\right)_{release}$ from Eq. (6) for the aluminum alloy, Al6061, the initial release wave speed ($C_R(\varepsilon_{init})$) was inferred from the C_R–u_p data provided in Vogler et al.[3] and the shear modulus ($G(\varepsilon)$) was inferred from the $G(p)$ plot provided in Peng et al.[41] As was done for SLG to derive Eq. (12), the $\left(\frac{dp}{d\varepsilon}\right)_{loading}$ for Al6061 is approximated to its post-yield stress Hugoniot slope ($\frac{d\sigma_h}{d\varepsilon}$) and is computed using the U_S–u_p data provided in Vogler et al.[3] Plots of $\left(\frac{dp}{d\varepsilon}(\varepsilon_{init})\right)_{release}$ and $\left(\frac{dp}{d\varepsilon}\right)_{loading}$ for Al6061 are shown in Fig. 14. The plot shown starts from $\varepsilon = \varepsilon_{HEL}$ in order to satisfy the prerequisite for evaluating Eq. (6). The ε_{HEL} for Al is inferred to be 0.006 from the data provided in Vogler et al.[3]

A similar plot of loading and release pressure–strain slopes for FS, which is the pure amorphous SiO_2, is provided here for comparison with SLG. To evaluate $\left(\frac{dp}{d\varepsilon}(\varepsilon_{init})\right)_{release}$ from Eq. (6) for FS, the initial release wave speed ($C_R(\varepsilon_{init})$) was inferred from the C_R–u_p data provided in Chhabildas and Grady,[13] and the shear modulus ($G(\varepsilon)$) was inferred from a polynomial interpolation of the $G(p)$ data, obtained as result of molecular dynamics (MD) simulation, in Schill et al.[15] As seen in Fig. 15, the $G(p)$ obtained from
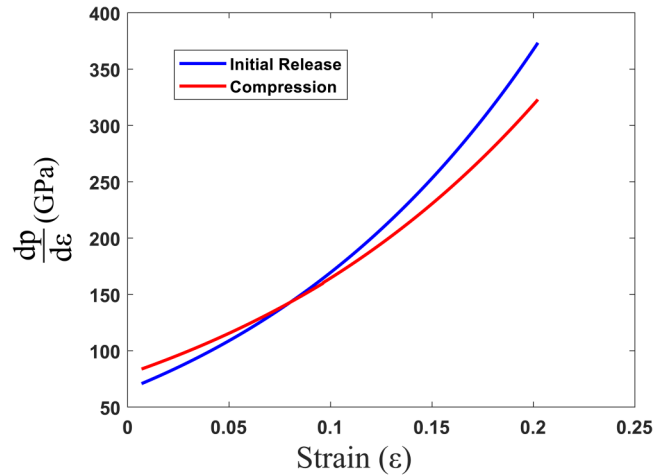
FIG. 14. Plots of the pressure–strain derivatives for Al 6061 subject to shock compression and release using data provided in Vogler et al.[3] and Peng et al.[41] The blue curve corresponds to $\frac{dp}{d\varepsilon}$ at initial release after shock compression to strains of ε. The red curve corresponds to the slope of the pressure Hugoniot as a function of compressive strain (ε). The plots start from strain corresponding to HEL, $\varepsilon_{HEL} = 0.006$. The uniaxial strain is computed as $(1 - \frac{\rho_0}{\rho})$.

MD simulations is in good agreement with the shear modulus obtained from static compression experiments at lower pressures (< 6 GPa). For FS, the generic trend in variation of elastic moduli (shear, longitudinal, and bulk) with pressure, as observed in Zha
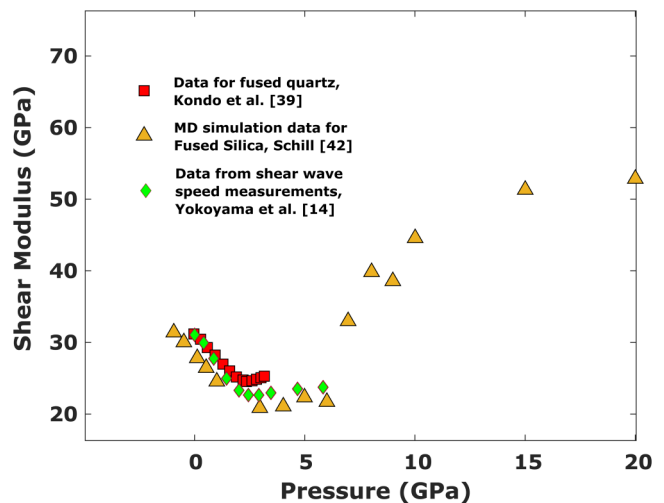
FIG. 15. Plot of shear modulus estimates for fused silica from static compression experiments (Kondo et al.[40] and Yokoyama et al.[16]) and from MD simulations (Schill et al.[43]). The shear modulus estimates from MD simulations can be seen to be in good agreement with the experimental findings. The MD estimates for shear modulus are available for pressures higher than 6 GPa as well and are hence used here.

et al.[42] as well, is that they first decrease with pressure, and after a certain threshold pressure start increasing again.

The ε_{HEL} for FS was inferred to be 0.16 from the data provided in Alexander *et al.*[28] The $\left(\frac{dp}{d\varepsilon}(\varepsilon)\right)_{loading}$ for FS was obtained from the loading pressure–strain plots provided in Schill *et al.*[15] The resulting $\left(\frac{dp}{d\varepsilon}(\varepsilon_{init})\right)_{release}$ and $\left(\frac{dp}{d\varepsilon}\right)_{loading}$ plots for FS are shown in Fig. 16. The plot shown starts from $\varepsilon = \varepsilon_{HEL}$ in order to satisfy the prerequisite for evaluating Eq. (6).

To evaluate $\left(\frac{dp}{d\varepsilon}(\varepsilon_{init})\right)_{release}$ from Eq. (6) for SLG, the initial release wave speed ($C_R(\varepsilon_{init})$) was inferred from Fig. 12, which demonstrates good agreement between the results of the current experimental work and those from previous experiments by Alexander *et al.*[11] The shear modulus [$G(\varepsilon)$] of SLG was approximated to be the same as that of FS. This is a reasonable assumption as the two materials have similar stiffness. This assumption was necessary as, to the authors' knowledge, there have been no static/dynamic experiments or MD simulations to study the variation of shear modulus of SLG with pressure. The value of ε_{HEL} for SLG is inferred to be 0.1 from Fig. 12. The $\left(\frac{dp}{d\varepsilon}(\varepsilon)\right)_{loading}$ for SLG is evaluated using Eq. (12). The resulting $\left(\frac{dp}{d\varepsilon}(\varepsilon_{init})\right)_{release}$ and $\left(\frac{dp}{d\varepsilon}\right)_{loading}$ plots for SLG are shown in Fig. 17. The plot shown starts from $\varepsilon = \varepsilon_{HEL}$ in order to satisfy the prerequisite for evaluating Eq. (6).

It can be seen from Fig. 14 that the pressure–strain derivatives for shock compression and for release are almost similar for Al6061, a material which is known to show regular ductile behavior (no phase transition). In clear contrast, Figs. 16 and 17 show that
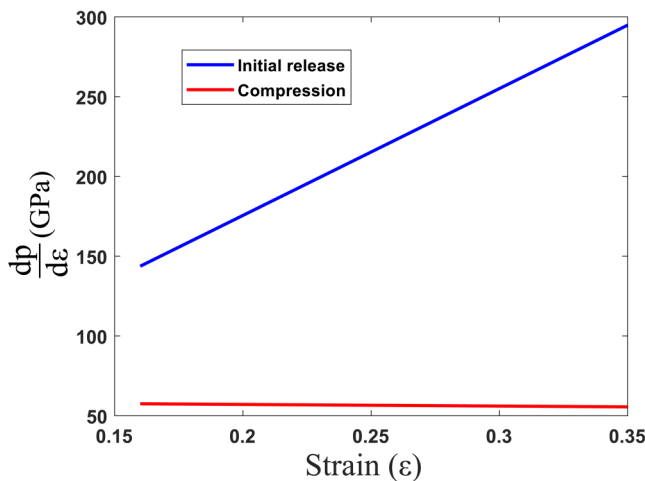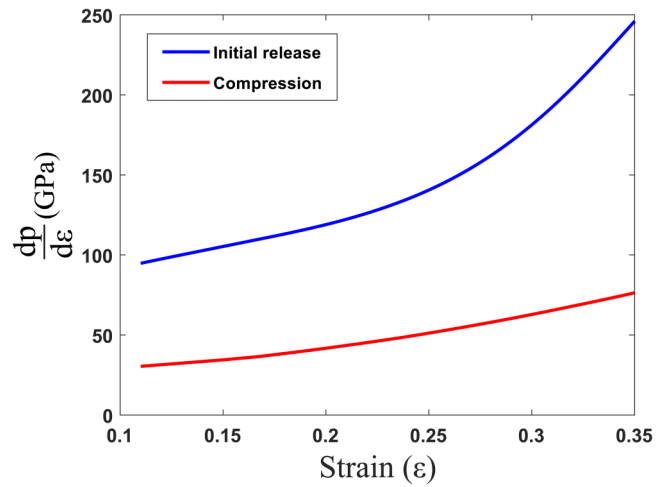

FIG. 17. Plots of the pressure–strain derivatives for SLG subject to shock compression and release. The blue curve corresponds to $\frac{dp}{d\varepsilon}$ at initial release after shock compression to strains of ε. The red curve corresponds to the slope of the pressure Hugoniot as a function of compressive strain (ε). The plots start from strains of $\varepsilon_{HEL} = 0.1$. The uniaxial strain is computed as $\left(1 - \frac{\rho_0}{\rho}\right)$.

the pressure–strain derivative is significantly higher for the initial release path as compared to the loading path, for both fused silica (FS) and soda-lime glass (SLG). Following the reasoning provided earlier, at the beginning of Sec. IV, these results thus provide a compelling indication for the existence of phase transition in FS and SLG.

It is noteworthy that in the work of Chhabildas and Grady,[13] it was suggested that the stiffer initial release observed from the stress–strain curves in shock and release experiments on fused quartz (same as fused silica) could be indicative of a phase transition in the material. However, that work[13] could not discern whether the behavior was due to a regular ductile behavior or due to an additional phase transition in the material. The current work has provided a more definitive evidence for the existence of phase transition in SLG and FS by demonstrating the mismatch between the loading and release paths in the pressure–strain curve, and not just the stress–strain curve. Furthermore, it is suggested that the failure wave phenomenon, which was observed to cause sudden densification in SLG,[17] is a phase transition wave in the material. Materials that undergo shock-induced phase transformations exhibit these phase transition waves.[38] In the case of SLG, the sudden densification that accompanies the phase transition is postulated to cause comminution of the material that it traverses,[17] thereby manifesting the so called "failure wave."

Although the mismatch in the loading and unloading (release) pressure–strain derivatives, as observed in Figs. 16 and 17, offer a clear evidence for the existence of phase transition, or some type of molecular rearrangement (such as change in coordination number) in FS and SLG, the destination phases, associated mechanisms, and the attendant kinetics of the transition are yet unclear. To shed further light on this, shock and release experiments on polycrystalline polymorphs of silica (such as coesite and α-quartz) are

FIG. 16. Plots of the pressure–strain derivatives for fused silica (FS) subject to shock compression and release. The blue curve corresponds to $\frac{dp}{d\varepsilon}$ at initial release after shock compression to strains of ε. The red curve corresponds to the slope of the pressure Hugoniot as a function of compressive strain (ε). The plots start from strains of $\varepsilon_{HEL} = 0.16$. The uniaxial strain is computed as $\left(1 - \frac{\rho_0}{\rho}\right)$.

necessary. This would help obtain an estimate for the pressure–strain derivatives under loading and release for these polymorphs, and further comparison of these results with the pressure–strain derivatives seen in Figs. 16 and 17 can provide insights into the destination phases and the kinetics involved. To the authors' knowledge, there are no available data for shock and release experiments on polycrystalline polymorphs of silica, like coesite, and α-quartz.

V. MODELING

The SLG shock and release plate impact experiments are modeled using ABAQUS/Explicit,[44] a commercial finite element analysis software used to model dynamic events. The simulations use a geometry shown schematically in Fig. 18, with 2D plane-strain rectangular elements. After checking for convergence with mesh-refinement, each element length is chosen to be $10\,\mu m$ thick along the X axis (shock loading direction) and $100\,\mu m$ wide along Y axis.[45] The SLG material in the simulation was divided into an "intact" and "failed" section with 5 GPa and zero spall strength, respectively.[17] This was done to emulate the behavior of the failure wave, which is known to travel at speeds of around 1.3 km/s in SLG[17] and is known to reduce the spall strength of the material behind the failure front to zero.

The strength of materials are modeled as a function of plastic strain (ε_p) and strain-rate $(\dot{\varepsilon}_p)$. The yield criterion is governed by J_2 plasticity, with yield (flow) strength (Y) given by

$$Y(\varepsilon_p, \dot{\varepsilon}_p) = (Y_0 + B\varepsilon_p^n)\left(1 + \left(\frac{\dot{\varepsilon}_p}{C\dot{\varepsilon}_{p0}}\right)^{\frac{1}{p}}\right). \tag{13}$$

2-D elements with plane strain condition

Diameter of disks = 34mm

Impactor

SLG Failed section (Zero spall Strength)

SLG Intact section (Spall strength = 5 GPa)

Nodes for which X-velocity history is recorded

LiF[100] window

Prescribed initial velocity
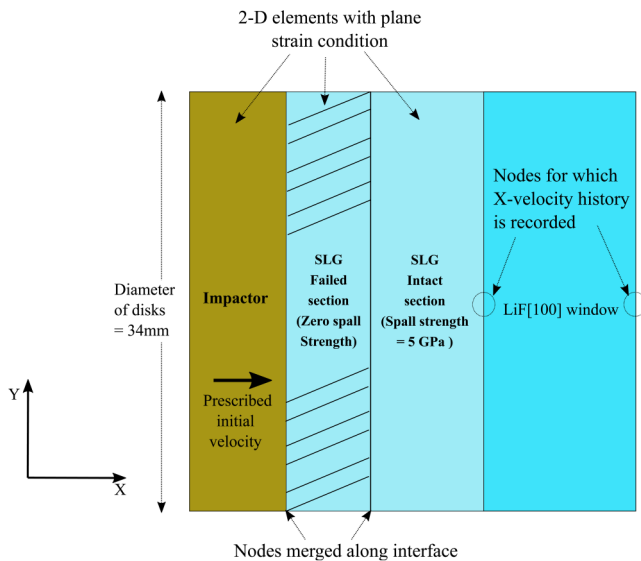
Nodes merged along interface

FIG. 18. Schematic of the geometry used to simulate shock and release experiments on SLG.

TABLE II. Properties of soda-lime glass used in the simulations.[17]

Density, ρ_0 (kg/m³)	Shear modulus, G (GPa)	Bulk modulus, K (GPa)	Grüneisen parameter, Γ_0
2480	30.5	45.3	5.06
Model parameters [Eq. (13)]			
Y_0 (GPa)	B (GPa)	n	C	P
6.1	1.0	0.8	900	2

The material properties and equation of state (EOS) used for SLG and WC are found in Joshi *et al.,*[17] and are summarized in Tables II and III, respectively. The LiF[100] window is modeled using the linear EOS, $U_s = C_0 + Su_p$, with parameters shown in Table IV. The shear modulus (G_0) for LiF is computed using a Poisson's ratio of 0.3[4] and a bulk modulus (K_0) of 70 GPa, which is assumed to be constant for the range of stresses simulated in this work. The bulk modulus was computed using the relation $K_0 = \rho_0 C_0^2$. The yield strength (Y_0) of LiF[100] was inferred from its HEL $(\approx 0.5\,GPa)$.[46] Owing to the small yield strength of LiF [100], hardening effects in the material are ignored for the range of stresses encountered in this work.

The shear modulus of SLG was assumed to be a constant (not a function of pressure) in the simulations. It would be more accurate to assume, for SLG, that the same shear modulus–pressure relation observed for fused silica (see Fig. 15). Such an assumed shear modulus–pressure relation for SLG would provide a more realistic estimate of the pressure (p) experienced by SLG as a function of its volumetric strain (see Figs. 4, 6, 8, and 10). However, the stress $[\sigma(\varepsilon)]$ estimate will remain unchanged, which would thus make the assumed shear modulus–pressure variation inconsequential to the final result of the simulation (e.g., SLG–LiF interface velocity history). It is, thus, most efficient to assume a constant shear modulus of 30.5 GPa[45] for SLG. The equation of state (EOS-1) and strength parameters used for SLG were similar to what was used in a previous work.[17] As before, the deviatoric stress was subtracted from the Hugoniot stress of EOS-1 to determine the increment in pressure as a function of volumetric compression (strain). The method for specifying the decrease in pressure (during release) as function of volumetric strain is described next.

TABLE III. Material properties of tungsten carbide (WC) used in the simulations.[47,48]

Density, ρ_0 (kg/m³)	Shear modulus, G (GPa)	Bulk modulus, K (GPa)	Model parameters [Eq. (13)]			
			Y_0 (GPa)	B (GPa)	n	C	P
15 480	273	379	4.3	9.2	0.38	1500	2
C_0 (m/s)	Grüneisen parameter, Γ_0		S	$\dot{\varepsilon}_{p0}(s^{-1})$		
4930	1.62		1.309	10^6		

TABLE IV. Properties of LiF[100] used in the simulation.[a]

Density, ρ_0 (kg/m³)	Shear modulus, G (GPa)	Yield strength, Y_0 (GPa)	Equation of state parameters		
			C_0 (m/s)	S	Grüneisen parameter (Γ_0)
2640	32.3	0.286	5150	1.35	1.7

[a]Equation of state properties were adapted from Oniyama[49] where Grüneisen parameter (Γ_0) is assumed to be ($2S-1$).

Figure 19 shows a plot of the evolution of Lagrangian release wave speeds as a function of volumetric strain for the different experiments analyzed in this work. For each of the experiments, the observed initial release wave speed is in good agreement with the best-fit curve provided in Alexander et al.[11] as shown in Fig. 12. After the initial release, the release wave speed first undergoes a steep decrease and eventually starts to decrease gradually with volumetric strain. This is similar to the behavior of LiF[100] observed in Ao et al.[4] and Liu et al.,[6] wherein the release wave speed underwent a steep reduction in the "quasi-elastic" section and transitioned to a more gradual "plastic/bulk" behavior. A schematic Lagrangian wave speed vs strain diagram depicting the aforementioned behavior of LiF[100] is shown schematically in Fig. 20. The length of the quasi-elastic segment was used to

estimate the strength of LiF[100] in Ao et al.,[4] with a smaller quasi-elastic segment corresponding to a smaller strength. Also, in the aforementioned works on LiF[100], it can be noticed that for plastic behavior (gradual reduction of release wave speeds), the release wave speeds were almost identical to the longitudinal compressive wave speeds. However, in the case of SLG, as observed in Fig. 19, the gradual release segment, though somewhat parallel to the compressive wave speed curve, had release wave speeds significantly higher than the longitudinal compressive wave speeds. This is another indicator that SLG does not undergo a simple elastic–inelastic transition and requires an additional phenomenon of phase transition to a stiffer phase to be considered to explain the observed behavior.

In Fig. 19, it can be observed that the onset of hysteresis (mismatch between loading and unloading wave speeds) precedes the elastic limit (HEL). This seems to be another peculiar behavior of SLG that could have been a cause for the largely varying estimates of its HEL in the past.[11,12]

The release wave speeds observed in Fig. 19 can be related to the derivative of stress as a function of strain: $\left(\frac{d\sigma}{d\varepsilon}\right)_{release} = \rho_0 C_R^2(\varepsilon)$. The derivative for pressure under release, $\left(\frac{dp}{d\varepsilon}\right)_{release}$, is obtained by subtracting the appropriate deviatoric term from the stress derivative. As stated earlier in this section, for the sake of simplicity in FEM simulations, without compromising the fidelity of the results, the shear modulus of SLG can be assumed to be a constant. Furthermore, as evidenced from the results in Figs. 4, 6, 8, and 10,
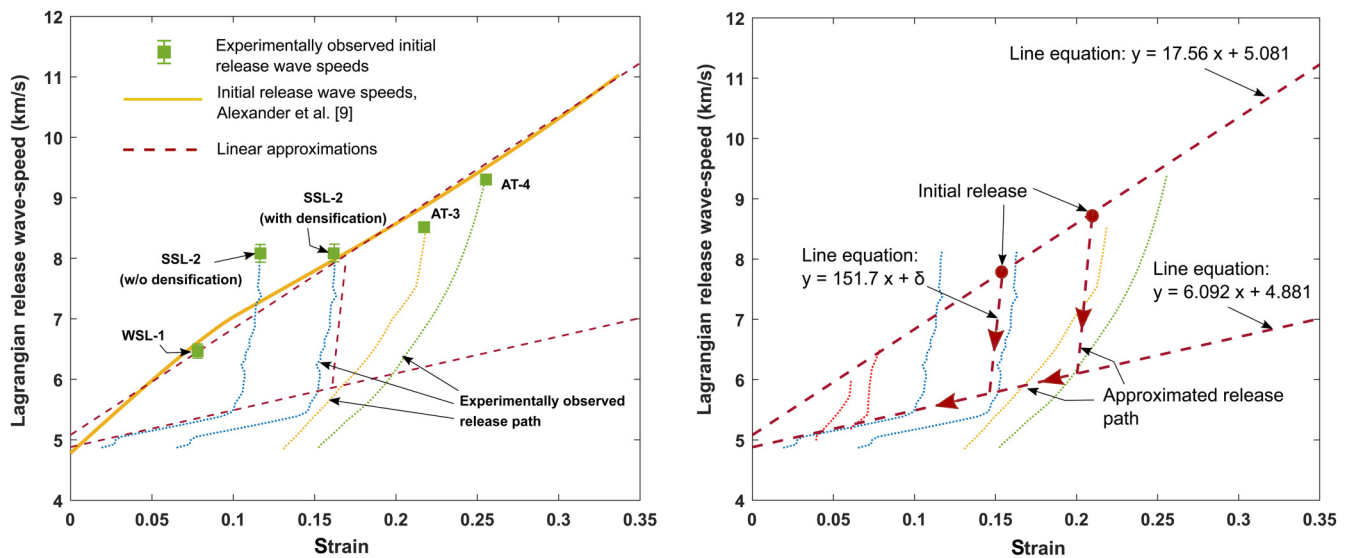

FIG. 19. Plots of experimentally observed evolution of release wave speeds in SLG compared with approximate linear estimates of the same used in modeling. (a) Plot of Lagrangian release wave speed evolution with strain observed in experiments. The initial release wave speed plot is the same as in Fig. 12 and is taken from Alexander et al.[11] The data for release paths for experiments AT-3 and AT-4 are taken from Alexander et al.[28] (b) Plot of approximate estimations of the release path for different peak compressive strains. This is used to model the evolution of release wave speed with strain in SLG. The δ in the equation for the high-slope release path denotes a variable intercept depending on the peak/initial release strain. The linear estimations for the release wave speeds are used only for initial compressive strains greater than the strain corresponding to the onset of hysteresis ($\varepsilon_{init} > 0.04$). The uniaxial strain is identical to the volumetric strain $\left(1 - \frac{\rho_0}{\rho}\right)$.
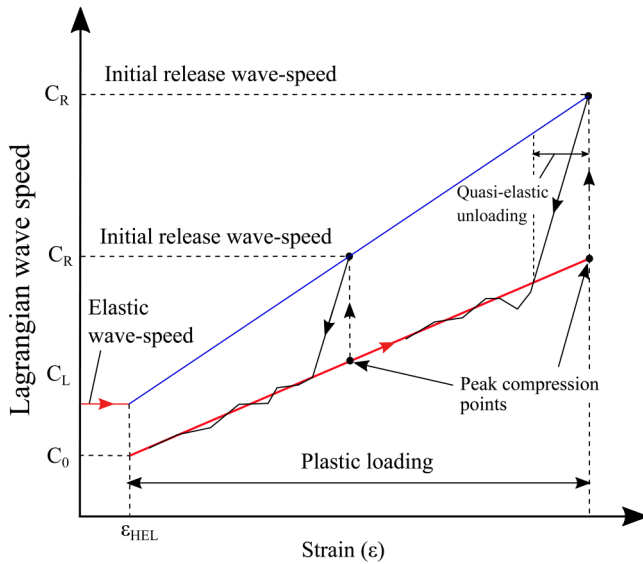
FIG. 20. Schematic Lagrangian wave speed vs strain diagram for a typical ductile material subject to shock compression and release. The uniaxial strain is computed as $\left(1 - \frac{\rho_0}{\rho}\right)$. The red line shows the evolution of the Lagrangian wave speed as the material undergoes compression (loading). For strains lower than the elastic limit (ε_{HEL}), the wave speed corresponds to the longitudinal elastic wave speed (C_L). For strains higher than ε_{HEL}, the plastic loading wave speeds evolves as shown in the figure, with C_0 obtained from the material's linear U_S–u_p relation: $U_S = C_0 + S u_p$. After reaching peak compression, at initial release (unloading), the material wave speed abruptly increases to a point on the "initial release velocity" line (shown in blue). With further release, the material wave speed proceeds along the quasi-elastic path (shown in black) and eventually merges with the plastic loading path. For SLG, it is observed that the release wave speeds always remain significantly higher than the loading wave speeds and never merges with the plastic loading path (see Figs. 12 and 19).

no reverse yielding occurs in SLG for the impact stresses accessed in the experiments. Thus, the pressure–strain derivative upon release can be expressed as

$$\left(\frac{dp}{d\varepsilon}\right)_{release} = \left(\frac{d\sigma}{d\varepsilon}\right)_{release} - \frac{4}{3}G = \rho_0 C_R^2(\varepsilon) - \frac{4}{3}G. \quad (14)$$

Thus, for peak compressive strains (ε_{init}) greater than the threshold for onset of hysteresis (see Fig. 12), the pressure release is prescribed using the data in Fig. 19(b) as follows:

$$\left(\frac{dp}{d\varepsilon}\right)_{release} = \max \begin{cases} \rho_0(151.7\varepsilon + \delta)^2 - \frac{4}{3}G, \\ \rho_0(6.092\varepsilon + 4.681)^2 - \frac{4}{3}G, \end{cases} \quad (15)$$

where $\delta = (17.56 - 151.7)\varepsilon_{init} + 5.081$ is dependent on the peak compressive strain, ε_{init}. The unit for density in the above equation is g/cc, for δ is km/s, and for the pressure-derivative and shear modulus is GPa. The release path prescribed in Eq. (15) alongside the loading path prescribed by EOS-1 and regular J_2 plasticity is

implemented using ABAQUS VUMAT for the SLG material. It is important to note that the release path prescribed in Eq. (15) is only for initial peak compressive strains greater than the threshold strain for onset of hysteresis ($\varepsilon_{init} > 0.04$). For initial peak compressive strains less than 0.04, an elastic release path is used in the simulations. This elastic release path is identical to the loading path described by EOS-1, discussed in Joshi et al.[17]

In contrast to the release path prescribed above, a separate set of simulations are also performed with regular release paths. In these simulations, the pressure–strain release path is identical to the pressure–strain loading path. Results for the SLG–LiF interface velocity obtained from the two sets of simulations are shown in Fig. 21, plotted alongside the optically corrected experimentally obtained interface velocity.

A. Discussion of simulation results

In simulating experiment No. WSL-1, an impact velocity of 490 m/s was assumed for the WC impactor, for all three simulations. It can be observed that the simulated SLG–LiF interface velocity profile adequately captures the peak velocity and the first release plateau. The timing of the initial release and a two-wave structure in the first release is also captured by the simulation that employed a release path prescribed by Eq. (15). However, the second velocity plateau is significantly overestimated by all simulations. The simulations also do not capture a two-wave structure that seems to be present in the second release as well. This could be due to a complicated second release behavior of SLG not accounted for in modeling the release or due to inadequate optical corrections in the experimental data after arrival of the shock wave at the LiF-free surface. Knowledge of the actual impact velocity, which was not observed due to lack of light return to the Down–Barrel probe, would have been useful to infer the existence and extent of a sudden densification due to the failure wave in SLG. The simulation using EOS-2 is able to capture the timing of the initial release but is unable to capture the two-wave nature of the first release.

For experiment No. SSL-2, it can be observed that the simulation using the prescribed release path seems to capture the experimentally observed peak velocity and initial release wave speed better than the simulation using regular elastic release. For experiment No. SSL-3, two simulations, employing equations of state EOS-1 and EOS-2,[17] respectively, were compared with the experimentally obtained (optically corrected) SLG–LiF interface velocity. Both simulations used the pressure release path prescribed in Eq. (15). Simulations for experiment No. SSL-3 using EOS-2, which accounts for densification due to failure waves in SLG, can be seen to have peak SLG–LiF interface velocities closer to the experimentally observed profile. As discussed in Joshi et al.,[17] unlike EOS-1, EOS-2 can capture the deficit in velocity that occurs due to the slower traveling failure wave. The densification caused by the failure wave, which is captured by EOS-2, and which is observed as a deficit in peak velocity,[17] serves as another indicator of a phase transition in SLG at these stresses. The experimentally observed initial release wave speed and wave structure are closely matched by both the simulations.

For experiment No. SSL-4, the simulation employing EOS-1 equation of state, with an elastic release path, captures accurately
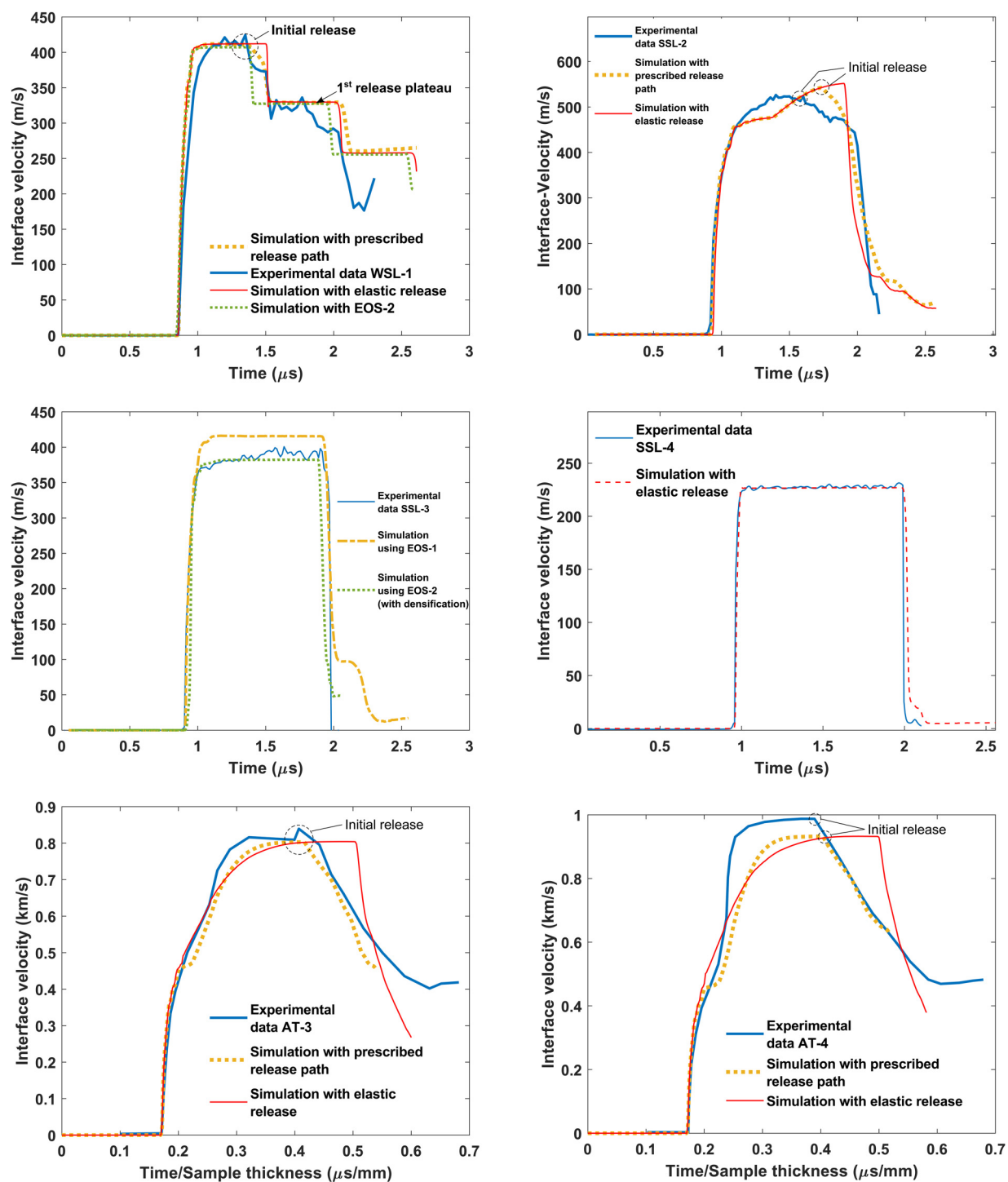
FIG. 21. Comparison of experimentally measured interface velocity (optically corrected) and simulation results. Data for experiments AT-3 and AT-4 were taken from Ref. 28. Results from two types of simulations are shown for most experiments. One set of simulations assumes a regular elastic unloading, and the other set of simulations involve a release path prescribed using Eq. (15). Alongside experimental results for experiment Nos. WSL-1 and SSL-3, one set of simulations use EOS-1 (without densification) and the others use EOS-2 (with densification). For experiment No. SSL-4, impact stresses involved were less than the assumed HEL[11] for SLG.

the peak SLG–LiF interface velocity and the initial release wave's speed and structure. As discussed earlier in Sec. V, simulations using the release path prescribed by Eq. (15) are used only for peak compressive strains greater than that required for onset of hysteresis ($\varepsilon_{init} > 0.04$). Thus, only the elastic release paths were used to model the stress unloading in experiment No. SSL-4. Simulations using EOS-2, which involves accounting for densification due to the failure wave, were not required to match the experimentally observed velocity profile as the impact stress in experiment No. SSL-4 was below the threshold to generate failure waves in SLG (i.e around 5 GPa[17]). The consistency between the experimental and simulation results again validates the optical correction applied to the observed SLG–LiF interface velocity data.

For experiment Nos. AT-3 and AT-4, the simulations using the release path prescribed by Eq. (15) capture accurately the experimentally observed initial release wave speed and the subsequent release path. Although simulations using the elastic release path result in a loading profile identical to simulations using a prescribed release path, the initial release wave speed is significantly underestimated by these simulations in both experiments. It can be observed that for experiment No. AT-4, both simulations result in peak velocities significantly less than the experimentally observed peak interface velocity. This could be because, as seen in Fig. 11, the EOS-1 curve used to model the compression response of SLG slightly underestimates the peak stress for experiment No. AT-4.

In summary, the results from the simulations demonstrate that employ an approximation for the path of evolution of the release wave speed (C_R) in the C_R–ε diagram [see Fig. 19(b)] is an effective means of modeling the release behavior of complex materials like SLG. For all experiments, the simulations using a release path prescribed by Eq. (15) capture the initial release wave speed and the release wave structure significantly better than the simulations using a regular elastic release path. As discussed earlier in Sec. V, the prescribed path in the Lagrangian release wave speed vs strain diagram (Fig. 19) has release wave speeds always significantly higher than the longitudinal compressive wave/bulk wave speed. Since wave speed is directly related to the slope of the pressure–strain curve, a higher release wave speed in comparison to the compressive/bulk wave speed, for a fixed strain, after the quasi-elastic release region, is indicative of a hysteresis in the pressure–strain curve, as would be expected of a phase transition (Sec. IV).

VI. CONCLUSION

Shock compression and release experiments have been performed to study the release behavior of SLG for 5–7 GPa impact stresses. Release to zero stress in SLG was achieved for the first time through symmetric impact and appropriate choice of thicknesses for the impactor and the target. Permanent densification and loading–unloading hysteresis, which was observed in three experiments, was seen to increase with impact stress. Furthermore, as shown in Sec. IV, the experimentally obtained stress–strain plots (Fig. 11), Lagrangian wave velocity plots [Figs. 12 and 19(a)] and shear modulus data from previous works (Fig. 15) reveal a hysteresis in the pressure–strain loading and unloading paths for FS and SLG, which serves as evidence for shock-induced phase transition in these materials.

The phase transition, which appears to start at around 5 GPa of impact stress, could also play an important role in the failure wave phenomenon observed in SLG shock compressed to these stresses. It is possible that kinetically hindered phase transitions are activated locally, at small length scales, thereby creating localized regions of densification. It was suggested in a previous work[17] that such localized densifications nucleate multiple microcracks, which merge to comminute the SLG material to create a "failed-section" of material behind the phase transition wave. Thus, the "failure wave" phenomenon observed in SLG and other normal silicate glasses could be a phase transition wave corresponding to the aforementioned phase transition.

Finally, based on the observed release wave speeds in SLG, a constitutive model to capture the release behavior of SLG subject to shock compression was proposed and evaluated. This methodology was able to adequately reproduce the key features of the experimentally observed velocity profile, such as the initial release wave speed, velocity deficit, and the release wave structure. The release wave speed vs strain diagram (Fig. 19) used for SLG, and its successful use in simulating the release behavior of SLG (Fig. 21), was seen to lend further support to the existence of a phase transition in the material for impact stresses higher than 5 GPa. The use of observed release wave speed vs strain plots obtained from shock compression and release experiments offer a possibly new tool to better model the complex release behavior of materials such as SLG or other materials that undergo phase transition under shock compression.

AUTHOR DECLARATIONS
Conflict of Interest

The authors have no conflicts to disclose.

APPENDIX: CALCULATING UNCERTAINTIES IN STRESS

Figure 22 shows the schematic of observed particle velocity vs time profile alongside profiles that account for an uncertainty in time of trigger. In all particle velocity–time plots, it is assumed that $t = 0$ corresponds to the actual time of impact. In the case that the actual impact precedes the observed trigger by a time of $\delta t/2$ (late trigger), the observed waveform must be shifted to the right by $\delta t/2$ (waveform 1) in order to set the time of impact to zero. In the case that the actual impact occurs $\delta t/2$ later than the observed trigger (early trigger), the observed waveform must be shifted to the left by $\delta t/2$ (waveform 2) to set the time of impact to zero. As shown in Fig. 22, waveform 2 would yield higher compressive and release wave speeds when compared to the observed waveform. Using Eq. (2), waveform 2 would thus result in a slightly higher compressive stress when compared to stresses obtained from the observed waveform. Similarly, waveform 1 would yield lower compressive and release wave speeds when compared to the observed
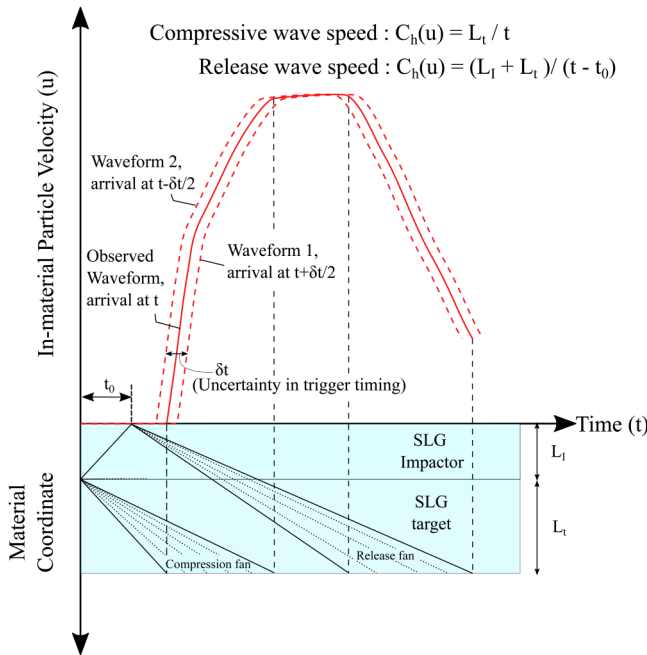
FIG. 22. Schematic of procedure to evaluate the wave speed in material frame, $C_h(u)$. The dotted lines represent the wave profiles considering a possible early trigger or late trigger. The uncertainty in time of trigger induces an uncertainty in the estimated wave speeds and hence the estimated stresses.
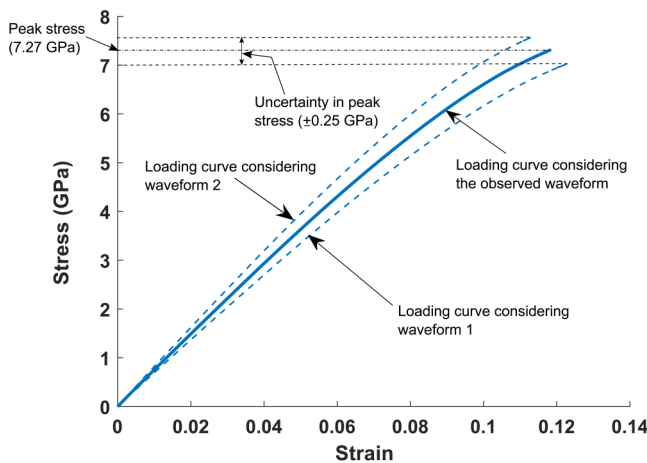

FIG. 23. Illustration of procedure to compute uncertainty in peak stress using results of experiment No. SSL-2. The higher loading stress branch corresponds to a trigger delay of 40 ns. The lower loading stress branch corresponds to a 40 ns early trigger. The uncertainty in the peak stress can be seen to be around 0.5 GPa (± 0.25 GPa). The uniaxial strain is computed as $\left(1 - \frac{\rho_0}{\rho}\right)$.

waveform. Using Eq. (2), waveform 1 would thus result in stresses slightly less compared to that obtained from the observed waveform.

Figure 23 shows an illustration of the above-mentioned procedure to compute the uncertainties in peak compressive stress for experiment No. SSL-2. A nominal uncertainty in trigger timing of 40 ns, corresponding to an impact tilt of around 1.2 mrad, was used. A similar procedure and value for the trigger timing uncertainty was used in Bauer et al.[33] The procedure for constructing the stress–strain curve from the optically corrected SLG–LiF interface velocity is outlined in Sec. II.

It can be seen that for experiment No. SSL-2 the peak stress is 7.27 GPa, and the uncertainty in stress, due to uncertainty in trigger, is around ± 0.25 GPa, which is a relative uncertainty of around 3.4%. This is very similar to the relative uncertainty of the trigger timing $\left(= \frac{0.04}{0.8} = 5\%\right)$. In contrast, the relative uncertainty in the particle velocities (see Table I) is around 0.01%, as computed using the procedure outlined by Dolan,[34] and a sampling window size of 40 ns. These relative uncertainty values are consistent with the claim that the uncertainty in trigger is the only significant source of uncertainty in the peak stress. This uncertainty in time of trigger can be minimized by minimizing the tilt in plane of impact.

DATA AVAILABILITY

The data that support the findings of this study are available within this article and from the corresponding author upon reasonable request.

REFERENCES

[1]J. R. Asay and J. Lipkin, "A self-consistent technique for estimating the dynamic yield strength of a shock-loaded material," J. Appl. Phys. **49**, 4242–4247 (1978).
[2]J. R. Asay, T. Ao, J.-P. Davis, C. Hall, T. J. Vogler, and G. T. Gray, "Effect of initial properties on the flow strength of aluminum during quasi-isentropic compression," J. Appl. Phys. **103**, 083514 (2008).
[3]T. J. Vogler, T. Ao, and J. R. Asay, "High-pressure strength of aluminum under quasi-isentropic loading," Int. J. Plast. **25**, 671–694 (2009).
[4]T. Ao, M. D. Knudson, J. R. Asay, and J.-P. Davis, "Strength of lithium fluoride under shockless compression to 114 GPa," J. Appl. Phys. **106**, 103507 (2009).
[5]M. A. Meyers, "Shock waves: Equations of state," in *Dynamic Behavior of Materials* (John Wiley & Sons, Ltd, 2007), pp. 124–151.
[6]Q. Liu, X. Zhou, X. Zeng, and S. N. Luo, "Sound velocity, equation of state, temperature and melting of LiF single crystals under shock compression," J. Appl. Phys. **117**, 045901 (2015).
[7]L. M. Barker and R. E. Hollenbach, "Laser interferometer for measuring high velocities of any reflecting surface," J. Appl. Phys. **43**, 4669–4675 (1972).
[8]O. T. Strand, D. R. Goosman, C. Martinez, T. L. Whitworth, and W. W. Kuhlow, "Compact system for high-speed velocimetry using heterodyne techniques," Rev. Sci. Instrum. **77**, 083108 (2006).
[9]N. K. Bourne and Z. Rosenberg, "The dynamic response of soda-lime glass," AIP Conf. Proc. **370**, 567–572 (1996).
[10]C. H. M. Simha and Y. M. Gupta, "Time-dependent inelastic deformation of shocked soda-lime glass," J. Appl. Phys. **96**, 1880–1890 (2004).
[11]C. S. Alexander, L. C. Chhabildas, and D. W. Templeton, "The Hugoniot elastic limit of soda-lime glass," AIP Conf. Proc. **955**, 733–738 (2007).
[12]D. P. Dandekar, "Optical and mechanical properties of soda lime glass under shock compression and release," Struct. Shock Impact IV WIT Trans. Built Environ. **25**, 439–448 (1996).

[13]L. C. Chhabildas and D. E. Grady, "Chapter IV: 6—Shock loading behavior of fused quartz," in *Shock Waves in Condensed Matter 1983*, edited by J. R. Asay, R. A. Graham, and G. K. Straub (Elsevier, Amsterdam, 1984), pp. 175–178.

[14]C. Meade and R. Jeanloz, "Effect of a coordination change on the strength of amorphous SiO_2," Science **241**, 1072–1074 (1988).

[15]W. Schill, S. Heyden, S. Conti, and M. Ortiz, "The anomalous yield behavior of fused silica glass," J. Mech. Phys. Solids **113**, 105–125 (2018).

[16]A. Yokoyama, M. Matsui, Y. Higo, Y. Kono, T. Irifune, and K.-I. Funakoshi, "Elastic wave velocities of silica glass at high temperatures and high pressures," J. Appl. Phys. **107**, 123530 (2010).

[17]A. Joshi, S. Ravindran, V. Gandhi, and G. Ravichandran, "Probing the properties and mechanisms of failure waves in soda-lime glass," J. Appl. Phys. **129**, 185902 (2021).

[18]R. J. Hemley, A. P. Jephcoat, H. K. Mao, L. C. Ming, and M. H. Manghnani, "Pressure-induced amorphization of crystalline silica," Nature **334**, 52–54 (1988).

[19]R. J. Hemley, C. T. Prewitt, and K. J. Kingma, "High-pressure behavior of silica, in *Silica*, (De Gruyter, 2018), Chap. 2, pp. 41-82.

[20]J. Wackerle, "Shock-wave compression of quartz," J. Appl. Phys. **33**, 922–937 (1962).

[21]A. E. Gleason, C. A. Bolme, H. J. Lee, B. Nagler, E. Galtier, D. Milathianaki, J. Hawreliak, R. G. Kraus, J. H. Eggert, D. E. Fratanduono, G. W. Collins, R. Sandberg, W. Yang, and W. L. Mao, "Ultrafast visualization of crystallization and grain growth in shock-compressed SiO_2," Nat. Commun. **6**, 8191 (2015).

[22]S. J. Tracy, S. J. Turneaure, and T. S. Duffy, "*In situ* x-ray diffraction of shock-compressed fused silica," Phys. Rev. Lett. **120**, 135702 (2018).

[23]P. Srivastava, K. Tanaka, B. Ramirez, and V. Gupta, "Stishovite nucleation at low shock pressures in soda-lime glass," Acta Mater. **215**, 117124 (2021).

[24]M. Pozuelo, J. Lefebvre, P. Srivastava, and V. Gupta, "Stishovite formation at very low pressures in soda-lime glass," Scr. Mater. **171**, 6–9 (2019).

[25]G. D. Mukherjee, S. N. Vaidya, and V. Sugandhi, "Direct observation of amorphous to amorphous apparently first-order phase transition in fused quartz," Phys. Rev. Lett. **87**, 195501 (2001).

[26]D. J. Lacks, "First-order amorphous-amorphous transformation in silica," Phys. Rev. Lett. **84**, 4629–4632 (2000).

[27]K. Trachenko and M. T. Dove, "Intermediate state in pressurized silica glass: Reversibility window analogue," Phys. Rev. B **67**, 212203 (2003).

[28]C. S. Alexander, L. C. Chhabildas, W. D. Reinhart, and D. W. Templeton, "Changes to the shock response of fused quartz due to glass modification," Int. J. Impact Eng. **35**, 1376–1385 (2008).

[29]R. V. Gibbons and T. J. Ahrens, "Shock metamorphism of silicate glasses," J. Geophys. Res. **76**, 5489–5498, https://doi.org/10.1029/JB076i023p05489 (1971).

[30]B. J. Jensen, D. B. Holtkamp, P. A. Rigg, and D. H. Dolan, "Accuracy limits and window corrections for photon Doppler velocimetry," J. Appl. Phys. **101**, 013523 (2007).

[31]A. Joshi, "A shock compression investigation of failure waves and phase transition in soda-lime glass," Ph.D. thesis (California Institute of Technology, 2021).

[32]L. Davison, "Fundamentals of shock wave propagation in solids," in *Shock Wave and High Pressure Phenomena* (Springer-Verlag, Berlin, 2008).

[33]S. Bauer, F. Bagusat, E. Strassburger, M. Sauer, and S. Hiermaier, "New insights into the failure front phenomenon and the equation of state of soda-lime glass under planar plate impact," J. Dyn. Behav. Mater. **7**, 81–106 (2021).

[34]D. H. Dolan, "Accuracy and precision in photonic Doppler velocimetry," Rev. Sci. Instrum. **81**, 053905 (2010).

[35]R. J. Clifton, "Analysis of failure waves in glasses," Appl. Mech. Rev. **46**, 540–546 (1993).

[36]D. Dandekar and P. Beaulieu, "Failure wave under shock wave compression in soda-lime glass," in *Metallurgical and Material Applications of Shock-Wave and High-Strain-Rate Phenomena* (Elsevier, 1995), pp. 211–218.

[37]R. J. Clifton, M. Mello, and N. S. Brar, "Effect of shear on failure waves in soda lime glass," AIP Conf. Proc. **429**, 521 (1998).

[38]J. K. Knowles and R. Abeyaratne, "Impact-induced transitions in two-phase elastic materials," in *Evolution of Phase Transitions: A Continuum Theory* (Cambridge University Press, Cambridge, 2006), pp. 59–82.

[39]D. B. McWhan, "Linear compression of α-quartz to 150 kbar," J. Appl. Phys. **38**, 347–352 (1967).

[40]K. Kondo, S. Iio, and A. Sawaoka, "Nonlinear pressure dependence of the elastic moduli of fused quartz up to 3 GPa," J. Appl. Phys. **52**, 2826–2831 (1981).

[41]J. Peng, F. Jing, D. Li, and L. Wang, "Pressure and temperature dependence of shear modulus and yield strength for aluminum, copper, and tungsten under shock compression," J. Appl. Phys. **98**, 013508 (2005).

[42]C.-S. Zha, R. J. Hemley, H.-k. Mao, T. S. Duffy, and C. Meade, "Acoustic velocities and refractive index of SiO_2 glass to 57.5 GPa by Brillouin scattering," Phys. Rev. B **50**, 13105–13112 (1994).

[43]W. Schill, "Variational and multiscale modeling of amorphous silica glass," Ph.D. thesis (California Institute of Technology, 2020).

[44]B. Hibbitt, B. Karlsson, and P. Sorenson, "ABAQUS/Explicit: User's Manual, Version 6.2," (Hibbitt, Karlsson and Sorenson Inc., Providence, RI, 2001).

[45]C. Kettenbeil, "Dynamic strength of silica glasses at high pressures and strain rates," Ph.D. thesis (California Institute of Technology, 2019).

[46]Y. M. Gupta, "Effect of crystal orientation on dynamic strength of LiF," J. Appl. Phys. **48**, 5067–5073 (1977).

[47]C. Kettenbeil, Z. Lovinger, T. Jiao, M. Mello, R. J. Clifton, and G. Ravichandran, "Inelastic behavior of tungsten carbide at high pressures," J. Mech. Phys. Solids **159**, 104762 (2022).

[48]S. Ravindran, V. Gandhi, Z. Lovinger, M. Mello, and G. Ravichandran, "Dynamic strength of copper at high pressures using pressure shear plate experiments," J. Dyn. Behav. Mater. **7**, 248–261 (2021).

[49]T. Oniyama, "Shock compression of molybdenum single crystals to high stresses," Ph.D. thesis (California Institute of Technology, 2020).